Cerebral Cortex, 2017; 1–18

doi: 10.1093/cercor/bhx260
Original Article

ORIGINAL ARTICLE

βAPP Processing Drives Gradual Tau Pathology in an Age-Dependent Amyloid Rat Model of Alzheimer’s Disease

Mickael Audrain[1,2,3,], Benoit Souchet[1,3,4,], Sandro Alves[1,3], Romain Fol[1,2,3], Arthur Viode[5], Alexis Haddjeri[6], Satoru Tada[1,3], Nicola S. Orefice[1,3], Charlène Joséphine[3,7], Alexis-Pierre Bemelmans[3,7], Thierry Delzescaux[3,7], Nicole Déglon[8,9], Philippe Hantraye[3,7,10], Yvette Akwa[11], François Becher[5], Jean-Marie Billard[6,], Brigitte Potier[6,], Patrick Dutar[6,], Nathalie Cartier[1,3] and Jérôme Braudeau[1,3]

[1]INSERM UMR1169, Université Paris-Sud, Université Paris-Saclay, Orsay 94100, France, [2]Université Paris Descartes, Paris, France, [3]CEA, DRF, Institut Francois Jacob, MIRCen, Fontenay-aux-Roses 92265, France, [4]Université Paris Saclay, Paris, France, [5]CEA, Institut Frédéric Joliot, Service de Pharmacologie et d’Immunoanalyse, 91191, Gif-sur-Yvette, France, [6]INSERM UMR894, Centre de Psychiatrie et Neurosciences, Université Paris Descartes, Sorbonne Paris Cité, Paris, France, [7]CNRS UMR9199, Fontenay-aux-Roses 92265, Université Paris-Sud, Université Paris-Saclay, Orsay 94100, France, [8]Department of Clinical Neurosciences, Laboratory of Cellular and Molecular Neurotherapies, Lausanne University Hospital, Lausanne, Switzerland, [9]Neuroscience Research Center, Laboratory of Cellular and Molecular Neurotherapies, Lausanne University Hospital, Lausanne, Switzerland, [10]INSERM UMS27, Fontenay-aux-Roses 92265, Université Paris-Sud, Université Paris-Saclay, Orsay 94100, France and [11]INSERM U1195 and Université Paris Sud and Université Paris-Saclay, 80 rue du général Leclerc, 94276 Le Kremlin-Bicêtre, France

Address correspondence to Jérôme Braudeau. Email: jerome.braudeau@agent-biotech.com.

Mickael Audrain and Benoit Souchet are joint first authors.
Jean-Marie Billard, Brigitte Potier and Patrick Dutar are contributed equally to this work. Nathalie Cartier and Jérôme Braudeau are contributed equally to this work.

Abstract

The treatment of Alzheimer’s disease (AD) remains challenging and requires a better in depth understanding of AD progression. Particularly, the link between amyloid protein precursor (APP) processing and Tau pathology development remains poorly understood. Growing evidences suggest that APP processing and amyloid-β (Aβ) release are upstream of Tau pathology but the lack of animal models mimicking the slow progression of human AD raised questions around this mechanism. Here, we described that an AD-like βAPP processing in adults wild-type rats, yielding to human APP, βCTF and Aβ levels similar to those observed in AD patients, is sufficient to trigger gradual Tauopathy. The Tau hyperphosphorylation begins several months before the formation of both amyloid plaques and tangle-like aggregates in aged rats and without associated inflammation. Based on a longitudinal characterization over 30 months, we showed that extrasynaptic and emotional impairments appear before long-term potentiation deficits and memory decline and so before Aβ and Tau aggregations. These compelling data allowed us to (1) experimentally confirm the causal relationship between βAPP processing and Tau pathology in vivo and without Tau transgene overexpression, (2) support the amyloidogenic cascade and (3) propose a 4-step hypothesis of prodromal AD progression.

Key words: Alzheimer's disease, amyloid pathology, hippocampus, pre-clinical AD, Tau pathology

Introduction

Alzheimer's disease (AD), the most common cause of dementia, is characterized by a progressive accumulation of β-amyloid peptide (Aβ), Tau hyper-, and abnormal phosphorylation, and displays a decline in cognitive functions followed by senile plaques and tangles formation. A large body of evidence suggest that there is a long infra-clinical phase of AD, in which pathological changes begin decades before classical hallmarks (senile plaques and neurofibrillary tangles) (Rajan et al. 2015). Evidence suggests that soluble Aβ peptides play a pivotal role during this infra-clinical phase (Ferreira et al. 2015). Toxicity of soluble Aβ directly affects synaptic plasticity even before amyloid plaque deposition and the formation of neurofibrillary tangles (Selkoe 2002; Selkoe and Hardy 2016). This infra-clinical phase has been poorly studied, despite increasing interest, largely due to the absence of pertinent animal models. Early stage animal models with a wide therapeutic window before amyloid and Tau deposition are highly needed, and would be more relevant in terms of human AD pathology than current transgenic models. Such models must fulfil specific requirements. First, the period prior to reaching an AD-like pathology is as essential as the full-blown disease. AD is an age-related disorder and models that display amyloid plaques or tangles too early in the life of the animal may not be relevant in terms of disease progression in humans (Kitazawa et al. 2012). Furthermore, most currently used AD models, generated over the last 20 years, are transgenic mice (Lee and Han 2013) and are based on very high transgene expression that hugely exceeds human levels (Audrain et al. 2016). Such overproduction is especially responsible for the supra-physiological release of amyloid peptides resulting in the early onset of histological brain lesions such as senile plaques, one of the hallmarks of AD. Several transgenic AD rat models have more recently been reported (Abbott 2004). Not only are rats widely used in toxicity studies, but their longer lifespan and their cognitive abilities makes them ideal for investigating the mechanisms of age-dependent neurodegenerative disease. The larger size of their brains (relative to mice) also facilitates translational procedures such as surgical procedures, magnetic resonance imaging, or positron emission tomography. Biological fluid collection such as plasma and cerebrospinal (CSF) is also simplified, reflecting the growing interest in the use of such models (Do Carmo and Cuello 2013). Strikingly, the gradual emergence of AD rat models has followed the same pattern as that for the prior development of transgenic mice in that they mostly focus on amyloid plaque formation. The first AD rat models did not develop senile plaques and were not considered to reproduce an AD phenotype (Echeverria et al. 2004; Ruiz-Opazo et al. 2004; Folkesson et al. 2007). A few years later, 2 transgenic Sprague Dawley rat models were developed in which amyloid plaques were triggered at 17 and 7 months of age (Flood et al. 2009). More recently, McGill-R-Thy1-amyloid protein precursor (APP) rats have been shown to display senile plaques as early as 6 months of age (Leon et al. 2010). A drawback of these more recently developed models is that they form senile plaques relatively early in life.

In this study, we developed and characterized an original rat model generated by AAV-mediated gene transfer (the AAV-AD rat) to induce the production of amyloid derivatives with levels as close as those found in human AD hippocampi and without a significant transgene overexpression. Soluble Aβ42 levels and the Aβ42/40 ratio gradually increased in rat hippocampi and decreased in CSF. Moreover, amyloid plaque deposition as cerebral amyloid angiopathy (CAA) progressively occurred until very late in the life of the animals, that is, 2.5 years after injection. More importantly, endogenous Tau was progressively both hyper- and abnormally phosphorylated over time, and associated with increased levels of GSK3β and DYRK1A kinases, resulting finally in phosphorylated Tau aggregate formation (AT8 and AT100 positive) in old rats. The biochemical, histological, electro-physiological, and behavioural evaluation of the AAV-AD rat highlighted the critical phases during infra-clinical disease progression implicated in AD and allowed us to propose a sequential AD progression hypothesis during infra-clinic stages, especially regarding βAPP processing and Tau pathology links before inflammation processes and misfolded protein pathologies (senile plaques and tangles).

Methods

Plasmid Design and Vector Production

We used a human double-mutant APP751 cDNA containing the Swedish and London mutations (codon optimized and containing a Kozak sequence; GeneArt, Life Technologies, Saint Aubin, France), and a human PS1 cDNA containing the M146L mutation (pENTR4-PS1-S182M146L). The APP_{SL} and the $PS1_{M146L}$ sequences were cloned into an AAV2 plasmid with a CAG promoter to generate AAV2-CAG-APP_{SL} or -CAG-$PS1_{M146L}$. AAV vectors were produced as previously described (Berger et al. 2015), except that the AAV packaging plasmid was replaced with a plasmid construct containing the rep gene of AAV2 and the cap gene of AAV9.

Animals

We used 130 male Wistar rats (8-week-old; SARL JanvierLabs, Le Genest Saint Isle, France) in this study. All experiments were conducted in accordance with the ethical standards of French and European regulations (European Communities Council Directive 2010/63/EU, authorization number APAFIS#4449-2016031012491697).

Bace 1 Inhibitor Study

Bace1 inhibitor LY2886721 was purchased from Apexbio Technology LLC, suspended in a DMSO/water mix (1:9) at 15 mg/mL, and orally administered by gavage in 1-month postinjected rats (15 mg/kg). Animals were killed 4 h later and tissues were collected as previously described. DMSO/water mix without the LY2886721 was used as vehicle for the control group.

Stereotactic Injections of AAVs

Rats were anesthetized by an intraperitoneal injection of ketamine/xylazine and placed in a stereotactic frame (Stoelting). Stereotactic intracerebral injections of AAVs into the hippocampi of both hemispheres were performed, using the following coordinates: antero-posterior: −3.6 mm, lateral: ±2.5 mm, ventral: −3.3 mm relative to bregma. We injected 4 μL of viral preparation into each site (2.5×10^{10} vg/site and 5×10^{10} vg/site for PS1 and APP, respectively) at a rate of 0.25 μL/min. Two groups of animals were initially created, according to the viral vectors injected or co-injected: AAV-CAG-PS1M146L (control rats), and AAV-CAG-APPSL + AAV-CAG-PS1M146L (AAV-AD rats).

Human Brain Samples

Postmortem samples were obtained from brains collected as part of the Brain Donation Program of the GIE-Neuro-CEB Brain Bank, Pitié-Salpêtrière Hospital, Paris, France. Autopsies were carried out by accredited pathologists, after informed consent had been obtained from the relatives, in accordance with French Bioethics laws. Five hippocampal samples from 5 patients with sporadic forms of AD (male and female; Braak 6/Thal 5; aged between 69 and 89 years, with a postmortem interval (PMI) of 30–59 h) and 5 hippocampus samples from 5 age-matched control subjects (male and female, aged between 69 and 92 years, PMI of 6–63 h) were used in this study (Table 1).

Tissue Collection and Sample Preparation

Rats were anesthetized with ketamine/xylazine and were first placed in a stereotactic frame to collect CSF by puncturing the cisterna magna with a low dead space syringe. One hemisphere was postfixed by incubation for 72 h in 4% PFA, cryoprotected in 30% sucrose in PBS, and cut into 40 μm sections with a freezing microtome (Leica) for histological analyses. The contralateral hemisphere was dissected for isolation of the hippocampus and cortex. Samples were homogenized in a lysis buffer (150 mM NaCl and 1% Triton in Tris-buffered saline) containing phosphatase (Pierce) and protease (Roche) inhibitors and centrifuged for 20 min at 15 000 ×*g*. The same procedure was applied to human samples.

ELISA

Extracted Aβ was quantified using the MSD Human Aβ42 V-PLEX Kit and the triplex Aβ Peptide Panel 1 (6E10) V-PLEX Kit (Meso Scale Diagnostics). Rat endogenous Aβ42 was assessed using the IBL Mouse/Rat Amyloid-beta (1-42) ELISA (IBL International GmbH). βCTF was quantified using the IBL APP βCTF Assay Kit (IBL International GmbH). Hyperphosphorylated Tau was quantified using the Innogenetics Phospho-Tau 181 P kit (Fujirebio Europe) and the MSD Phospho (Thr231)/Total Tau Kit (Meso Scale Diagnostics). The ELISA was performed according to the kit manufacturer's instructions in each case.

Western Blotting

Equal amounts of protein (30 μg) were separated by electrophoresis in NuPAGE Bis-Tris Gels (Life Technologies) and transferred to nitrocellulose membranes. The membranes were hybridized with various primary antibodies: APP 6E10 (1/500, Covance), PS1 (1/1000, Millipore), APP C-ter (1/500, Millipore), GAPDH (1/1000, Abcam), P-Tau Thr 212 (1/1000, Invitrogen), P-Tau Thr 422 (1/1000, Invitrogen), CDK5 (1/1000, Abcam), GSK3β (1/1000, Abcam), DYRK1A (1/250, Abnova), P-CamkII Thr 286 (1/1000, Abcam), GFAP (1/500, DAKO). Various secondary antibodies were also used: ECL horseradish peroxidase linked anti-rabbit, ECL horseradish peroxidase linked Anti- mouse, ECL horseradish peroxidase linked anti-rat (all 1/2000, GE Healthcare) (Table 2).

Immunohistochemistry and Image Acquisition

Cryosections were washed with 0.25% Triton in PBS and saturated by incubation (0.25% Triton in PBS/5% goat serum). They were then incubated with one or more of the following primary antibodies: APP C-ter, (1/500, Millipore), 4G8-Biotin (1/1000, Covance), 6E10 (1/500, Covance), BAM10 (1/500, ThermoFisher), CD31 (1/200, Abcam), AT8 P-Tau pSer202/Thr205 (1/1000, ThermoFischer), and AT100 P-Tau pThr212/Ser214 (1/1000, ThermoFisher). For nonfluorescent immunostainings, endogenous peroxidase was quenched with PBS containing 3% H_2O_2 for 5 min followed by amplification using the ABC system (VECTASTAIN Elite ABC HRP Kit, Vector Laboratories). Horseradish peroxidase conjugate and 3,3′-diaminobenzidine were then used according to the manufacturer's manual

Table 1 Details of human brain samples used.

	Gender	Age (years)	PMI (hours)	Clinical AD status	Diagnosis
	M	73	54	Braak V, Thal IV, CAA	AD
	F	89	59	Braak VI, Thal V, CAA	AD
	M	70	30	Braak VI, Thal V, CAA	AD
	M	69	30	Braak VI, Thal V, CAA	AD
	M	72	44	Braak VI, Thal V	AD
Mean	M (80%)	74.6	43.4	Braak VI, Thal V, CAA	AD
	F	92	21	Braak I	Ctrl
	M	58	6	Braak I-II	Ctrl
	M	82	63	Braak II, Thal I	Ctrl
	F	89	12	/	Ctrl
	M	69	6	/	Ctrl
Mean	M (60%)	74.5	21.75	Braak I, Thal I	Ctrl

Table 2. Table of used antibodies.

Detected antigen	Antibodies	Dilution/technique	Suppliers
Human APP (6E10)	Purified anti-β-Amyloid, 1-16 Antibody	1:500/WB	Biolegend
Total APP (APP Cter)	Anti-APP A4 Antibody, a.a. 66–81 of APP {NT}, clone 22C11	1:500/WB	Millipore
PS1	Anti-Presenilin-1 Antibody, loop, a.a. 263–378, CT, clone PS1-loop	1:1000/WB	Millipore
GAPDH	Anti-GAPDH antibody [6C5] (ab8245)	1:1000/WB	Abcam
p-CAMKII Thr286	Anti-CaMKII (phospho T286) ab32678	1:500/WB	Abcam
rodent APP (4 G8)	Purified anti-β-Amyloid, 17–24 Antibody	1:250/IH	Covance
Human APP (6E10)	Purified anti-β-Amyloid, 1–16 Antibody	1:250/IH	Covance
BAM10	beta Amyloid Monoclonal Antibody (BAM10)	1:250/IH	Thermo Scientific
CD31	Anti-CD31 antibody [EPR3094] (ab76533)	1:100/IH	Abcam
p-TAU Ser422	Phospho-Tau (Ser422) Polyclonal Antibody 44-764 G	1:1000/WB	Thermo Scientific
p-TAU Thr212	Phospho-Tau (Thr212) Antibody (44-740 G)	1:1000/WB	Thermo Scientific
AT8	Phospho-Tau (Ser202, Thr205) Monoclonal Antibody (AT8)	1:500/WB	Millipore
AT100	Phospho-Tau (Thr212, Ser214) Monoclonal Antibody (AT100)	1:500/WB	Millipore
GSK3β	Anti-GSK3 beta antibody (ab73173)	1:500/WB	Abcam
DYRK1A	DYRK1A monoclonal antibody (M01), clone 7D10	1:250/WB	Abnova
CDK5	Anti-Cdk5 antibody [EP715Y] (ab40773)	1:1000/WB	Abcam
AT8	Phospho-Tau (Ser202, Thr205) Monoclonal Antibody (AT8)	1:250/IH	Millipore
AT100	Phospho-Tau (Thr212, Ser214) Monoclonal Antibody (AT100)	1:100/IH	Millipore

(Vector® DAB, Vector Laboratories). Images were captured using a Nikon Eclipse Ti Microscope or a Leica TCS SP8 confocal microscope and analysed using ImageJ software (NIH).

3D Reconstruction

In order to visualize 3D organization at cellular level, several image processing steps were performed using BrainVISA software (http://brainvisa.info). Series of images acquired with the confocal system were first stacked to produce 3D images and objects of interest were segmented. Based on the high contrast available in the images of fluorescence, an adaptive threshold followed by a median filtering operation were realized under expert supervision to produce proper binary segmentations. In the last step, surfaces were derived from these segmentations to generate 3D views of both cells and pathological aggregates enabling to assess accurately their spatial organization in 3D.

LC-MS/MS Analyses

Sample preparation was adapted from Barthelemy et al. (2016). Briefly, 20 μL of 70% perchloric acid were added to 20 μL of hippocampal extracts for protein precipitation. Samples were kept on ice for 15 min before centrifugation (15 min, 4 °C, and 16 000 g). Supernatants were collected and mixed with 40 μL of 1% trifluoroacetic acid (TFA) before μSPE extraction on Oasis HLB sorbent. Samples were loaded and washed with 500 μL of 0.1% TFA in 10% acetonitrile on the sorbent, previously conditioned and equilibrated. Tau proteins were eluted with 100 μL of 27.5% acetonitrile in 0.1% TFA. Extracts were evaporated to dryness with a Turbovap instrument (Biotage) (10 psi of nitrogen, 50 °C, 2 h). Samples were reconstituted with 35 μL of 50 mM ammonium bicarbonate and digested overnight at 37 °C with 5 μL of 100 ng/μL trypsin solution (sequencing grade modified trypsin, Promega, Madison, WI) in 50 mM ammonium bicarbonate. Finally, the digest was acidified with 5 μL of 1 M chloridric acid and used for subsequent LC-MS/MS analyses following addition of 2.5 ng of the 3 labeled PEPotec peptides.

Capillary LC-HRMS was performed on an Ultimate 3000 chromatography system coupled to a Q-Exactive Quadrupole-Orbitrap mass spectrometer (Thermo Fisher Scientific). Ten microliters of the sample extract were injected and loaded for 3 min at a flow rate of 10 μL/min on a μPrecolumn C18 Pepmap100 (0.3 mm × 5 mm, 5 μm) (Thermo Scientific). Peptide separation was achieved in 60 min using an Acclaim Pepmap RSCL C18-100A column (0.3 mm × 150 mm, 2 μm) (Thermo Scientific) at a flow rate of 6 μL/min. The column oven temperature was set to 35 °C. The mobile phases were (A) 0.1% formic acid in water and (B) 0.1% formic acid in 80% MeOH. After an isocratic step of 3 min at 4% phase B, a linear gradient from 4% to 55% B was run for 30 min, then increased to 90% B. An equilibration step was performed at 4% B for 20 min. Data were acquired in the positive ion mode with an ion spray voltage of 4 kV, a capillary temperature set to 320 °C, and sheath gas at 5. S-lens RF were set at 60. The AGC target was set to 1e6 and Orbitrap resolution to 70 000 at 200 m/z for all experiments.

A time-scheduled sequential PRM method was established targeting the following p-tau peptides corresponding to Tau protein phosphorylation on residues Ser202, Thr217, Thr231/Ser235 (Table 3). The signal of up to 11 major and noninterfered fragment ions identified with high resolution from a common peptide precursor were summed up to provide one extracted ion chromatogram (XIC) for each p-tau peptide (Fig. 7C). Isotope-labeled synthetic peptides with labeled amino acids lysine (K, label 13C615N2) or arginine (R, label 13C615N4) were used for signal normalization and relative quantification of p-tau peptides. Raw mass spectrometry data were exported to Skyline 3.7 for verification of the transitions ratio of unlabeled and labeled peptides. Xcalibur 2.2 software (Thermo Fisher Scientific) was used for quantitative data analysis.

Behavioural Assessment

Open-field: The apparatus consisted of an open-topped, clear plexiglas box measuring 90 × 90 × 70 cm placed in a room with controlled dim lighting (40 lux) and constant white noise at 40 dB. The rats were placed in the centre of the arena and a video recording was made over a period of 5 min. The behaviour of the animals was analysed from this video. The arena was divided into a central region and a peripheral region, and the time spent in the centre and periphery of the open-field was measured.

Morris water maze: Experiments were performed in a tank of 180 cm in diameter and 50 cm deep, filled with opacified water

Table 3. MS parameters for LC-MS/MS analysis of Ser 202; Thr 217 and Thr231/Ser235 as well as their corresponding labeled peptides.

Peptide sequence	Precursor ion m/z	Product ion m/z	Normalized collision energy %	Retention time (min)
SGYSSPGsPGTPGSR	737.30 (z = 2)	1166.4838 (y12) 1079.4517 (y11) 992.4197 (y10) 895.3669 (y9) 838.3455 (y8) 671.3471 (y7) 416.2252 (y4) 496.7135 (y10 + 2) 308.1241 (b3)	22	17.7
SGYSSPGSPGtPGSR[$^6C_{13}$; $^4N_{15}$]	742.31 (z = 2)	1176.4920 (y12) 1089.4600 (y11) 1002.4280 (y10) 905.3752 (y9) 848.3537 (y8) 761.3217 (y7) 426.2335 (y4) 501.7176 (y10 + 2) 308.1241 (b3)	22	17.7
TPSLPtPPTREPK	500.92 (z = 3)	1399.6981 (y12) 1102.5293 (y9) 824.4625 (y7) 727.4097 (y6) 630.3570 (y5) 529.3093 (y4) 700.3527 (y12 + 2) 651.8263 (y11 + 2) 608.3103 (y10 + 2) 551.7683 (y9 + 2) 467.2376 (y12 + 3)	22	23.2
TPSLPtPPTREPK[$^6C_{13}$; $^2N_{15}$]	504.26 (z = 3)	1409.7064 (y12) 1112.5375 (y9) 834.4707 (y7) 737.4180 (y6) 640.3652 (y5) 539.3175 (y4) 705.3568 (y12 + 2) 656.8304 (y11 + 2) 613.3144 (y10 + 2) 556.7724 (y9 + 2) 470.5736 (y12 + 3)	22	23.2
VAVVRtPPKsPSSAK	561.95 (z = 3)	978.4656 (y9) 792.8810 (y14 + 2) 743.8925 (y14–98 + 2) 757.3624 (y13 + 2) 708.3740 (y13–98 + 2) 489.7364 (y9 + 2) 440.7480 (y9–98 + 2) 706.3648 (b6)	22	16.5
VAVVRtPPKSPSsAK[$^6C_{13}$; $^2N_{15}$]	564.6173 (z = 3)	986.4798 (y9) 796.8881 (y14 + 2) 747.8996 (y14–98 + 2) 761.3695 (y13 + 2) 712.3811 (y13–98 + 2) 493.7435 (y9 + 2) 444.7551 (y9–98 + 2) 706.3648 (b6)	22	17.3

kept at 21 °C, and equipped with a platform of 18 cm in diameter, submerged 1 cm below the surface of the water. Visual clues were positioned around the pool and the luminosity was maintained at 350 lux. The rats were initially exposed to a learning phase, which consisted of daily sessions (3 trials per session) on 5 consecutive days. The starting position varied pseudo-randomly, between the 4 cardinal points. A mean interval of 20 min was left between trials. The trial was considered to have ended when the animal reached the platform. Long-term spatial memory was assessed 72 and 120 h after the last training trial in a probe trial in which the platform was no longer available. Animals were monitored using EthoVision software.

Ex Vivo Electrophysiology

Rats were anesthetized with halothane and decapitated. The brain was rapidly removed from the skull and placed in chilled (0–3 °C) artificial cerebrospinal fluid (ACSF) containing 124 mM NaCl, 3.5 mM KCl, 1.5 mM MgSO4, 2.5 mM CaCl2, 26.2 mM NaHCO3, 1.2 m4M NaH2PO4, 11 mM glucose. Transverse slices (300–400 μm thick) were cut with a vibratome and placed in ACSF in a holding chamber, at 27 °C, for at least 1 h before recording. Each slice was individually transferred to a submersion-type recording chamber and submerged in ACSF continuously superfused and equilibrated with 95% O_2, 5% CO_2.

Tonic current: The biophysical properties of the tonic current generated by the activation of extrasynaptic NMDA receptors with ambient glutamate were evaluated. Whole-cell patch-clamp recordings of CA1 pyramidal cells were performed at room temperature, with borosilicate patch pipettes (5 MΩ) filled with a buffer containing 140 mM CsCH4O3S, 6 mM CsCl, 2 mM MgCl2, 10 mM HEPES, 1.1 mM EGTA, 5 mM QX-314 5, and 4 mM ATP, at a pH of 7.3 at 290 mosm. Transmembrane currents were acquired and filtered through an amplifier (AxoPatch 1-D, Axon Instruments), stored on a computer, and digitized using WinLTP software for analysis. The tonic current was recorded at a holding potential of +40 mV, in the presence of TTX (1 μM), NBQX (10 μM), and bicuculline (10 μM), to isolate the NMDA component of the holding current (hc). After recording oa stable control hc for 3–5 min, APV (50 μM) was added to the superfusion medium. The hc fell to a new stable value under the effect of APV, and the difference between the control hc and its value in the presence of APV determined the amplitude of the tonic current.

Long-term potentiation (LTP) and depression (LTD). For the LTP, theta-burst stimulation (TBS), mimicking the natural stimulation at the theta frequency from the medial septum to the hippocampus, consisted of 5 trains of four 100 Hz pulses each, separated by 200 ms and delivered at the test intensity. The sequence was repeated 3 times, with an interburst interval of 10 s. Testing with a single pulse was resumed for 60 min (TBS) to determine the level of LTP. The LTD was induced by the application of low frequencies stimulation (LFS): 1 Hz for 15 min or 2 Hz for 10 min. Responses were recorded for at least for 45 min after LFS.

Statistical Analysis

Data are expressed as the mean ± SEM. Statistical analyses were performed using GraphPad Prism (GraphPad Software) or Statistica (StatSoft, Inc.) software and the statistical significance was set to a *P*-value < 0.05 for all tests. One-way ANOVA followed by Tukey's post hoc test or 2-way ANOVA followed by Sidak's post hoc test were used to determine the significance of differences between groups. Student's *t*-test was used when only 2 groups were analysed.

Results

AAV-AD Induction in Wild-Type Adult Rat Hippocampi

We generated AAV vectors encoding human mutant $PS1_{M146L}$ and human mutant APP_{SL} (Swedish & London mutations) that were bilaterally co-injected into the stratum lacunosum of the hippocampus of 8-week-old male Wistar rats (Fig. 1A). We used the AAV9 capsid known to efficiently transduce the hippocampus (Fol et al. 2015; Alves et al. 2016). We injected AAV-AD rats ($n = 8$) with both APP_{SL} and $PS1_{M146L}$ AAV constructs, whereas the control group ($n = 4$) was only injected with the AAV-PS1 virus. We evaluated vector-mediated APP and PS1 expression in the hippocampus 1-month later. Western blot analysis of whole hippocampal extracts revealed comparable PS1 full-length (PS1 FL) levels in injected and non-injected rats. A 30-kDa PS1 N-terminal fragment (PS1 NTF) was mostly detectable in injected hippocampi, confirming the formation of the PS1 active site responsible for the formation of Aβ species, without PS1 FL accumulation. Similarly, human APP was expressed from 1-month after injection without a significant increase of total APP (human + rat forms; Fig. 1B). We assessed the engagement of the amyloidogenic pathway by first confirming the production of βCTF (C99 fragment; Control: 6.20 ± 0.97 pMol/L; AAV-AD: 11.28 ± 0.31 pMol/L; 1-way ANOVA followed by Tukey's post hoc test: P = 0.012), the first cleavage product of APP by BACE1 (Fig. 1C) (Hardy and Higgins 1992). We also confirmed that AAV-AD induction resulted in the substantial release of both soluble Aβ40 (Control: 1.25 ± 1.25 pg/mL; AAV-AD: 14.31 ± 1.46 pg/mL; 1-way ANOVA followed by Tukey's post hoc test: P = 0.0001) and Aβ42 peptides (Control: 0.25 ± 0.25 pg/mL; AAV-AD: 6.78 ± 0.68 pg/mL; one-way ANOVA followed by Tukey's post hoc test: $P = 0.0001$) relative to control rats (Fig. 1*D*,*E*). Aβ levels in the cerebrospinal fluid (CSF) of AD patients has a diagnostic potential as a biomarker (Dubois et al. 2014). We evaluated the dispersion of both Aβ peptides from the hippocampus to the CSF 1-month after injection. Despite the expected absence of βCTF in the CSF (data not shown), AAV-AD induction led to an increase of both Aβ40 (Control: 0.94 ± 0.34 pg/mL; AAV-AD: 6.00 ± 1.03 pg/mL; 1-way ANOVA followed by Tukey's post hoc test: $P = 0.007$) and Aβ42 (Control: 0.35 ± 0.09 pg/mL; AAV-AD: 5.46 ± 0.97 pg/mL; 1-way ANOVA followed by Tukey's post hoc test: $P = 0.009$) levels in CSF (Fig. 1F,G). We administered the β-secretase (also known as BACE) inhibitor, LY2886721, diluted in DMSO, by gavage in 1-month postinjected AAV-AD rats to confirm the involvement of BACE in AAV-AD induction. We observed a complete inhibition of βCTF production 4 h after gavage (Fig. 1C; LY2886721-treated AAV-AD: 7.06 ± 0.65 pMol/L; 1-way ANOVA followed by Tukey's post hoc test: $P = 0.008$) confirming BACE1-dependent βCTF production. In agreement with the amyloidogenic cascade hypothesis (Hardy and Higgins 1992), decreasing βCTF levels also led to decreases in both Aβ40 (LY2886721-treated AAV-AD: 4.40 ± 0.99 pg/mL; 1-way ANOVA followed by Tukey's post hoc test: $P < 0.0001$) and Aβ42 (LY2886721-treated AAV-AD: 2.30 ± 0.41 pg/mL; one-way ANOVA followed by Tukey's post hoc test: $P < 0.0001$) production (Fig. 1*D*,*E*). In a similar manner, both Aβ40 (LY2886721-treated AAV-AD: 3.23 ± 0.49 pg/mL; one-way ANOVA followed by Tukey's post hoc test: P = 0.04) and Aβ42 (LY2886721-treated AAV-AD: 2.25 ± 0.57 pg/mL; 1-way ANOVA followed by Tukey's post hoc test: $P = 0.02$) levels decreased in CSF 4 h after gavage with LY2886721 (Fig. 1F,G). Altogether, these data indicate BACE1-dependent engagement of the amyloidogenic cascade from 1-month postinjection. In addition, a positive linear correlation between hippocampal and CSF Aβ42 levels (Pearson correlation coefficient test: $P = 0.0051$, $r^2 = 0.56$; Fig. 1*H*) suggests that Aβ42 may passively spread from the hippocampus to the CSF.

AAV-AD Induction Leads to Progressive Cognitive Impairment

We evaluated whether human-like APP processing in AAV-AD rats is associated with progressive cognitive and behavioural

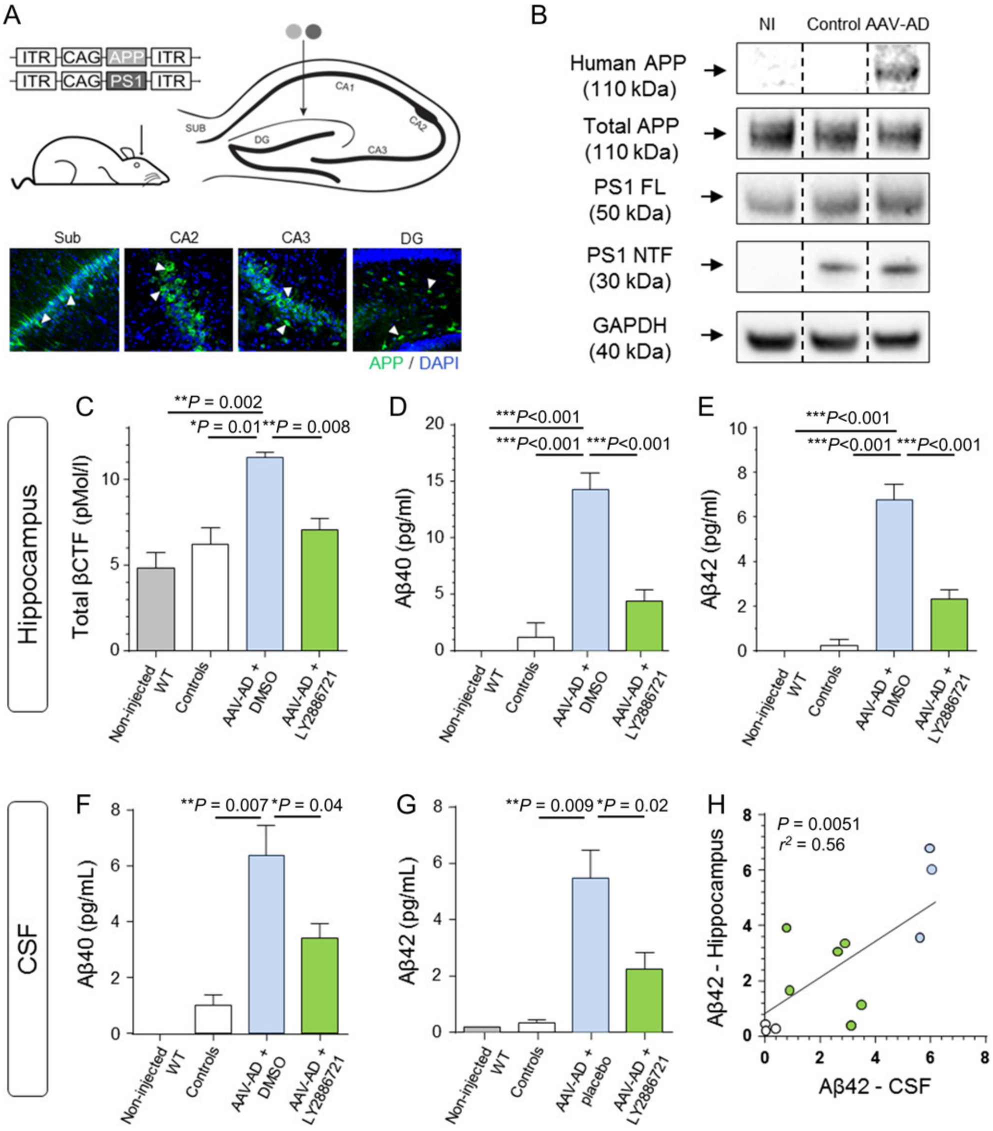

Figure 1. AAV-AD induction leads to BACE1-dependent APP processing in the hippocampus of adult rats. We generated AAV vectors encoding mutated human PS1M146L and mutated human APPSL, and injected them bilaterally into the stratum lacunosum of the rat hippocampus. Rats received either the AAV-CAG-PS1M146L vector (control, $n = 4$) or both AAV-CAG-PS1M146L and AAV-CAG-APPSL vectors (AAV-AD, $n = 8$). Rats were killed 1-month after vector injection for transgene expression analysis in the hippocampus. (*A*) Upper panel: schematic representation of the injection site in the rat hippocampus. Bottom panel: Confocal microscopy acquisition performed in sections from AAV-AD hippocampus: human APP (green) was expressed in sparse neurons in CA2/CA3 layers (blue) but also in the subiculum (Sub) and dentate gyrus (DG) subfields (APP C-ter antibody). (*B*) Representative western blots showing the expression of human APP (6E10 antibody), total APP (rat + human forms; APP C-ter antibody) and PS1 (full-length: PS1 FL and N-terminal fragment: PS1 NTF), confirming transgene expression 1-month after injection. All western blots were performed on whole hippocampal extracts (TBS-Tx soluble fraction). (*C–E*) Comparative analysis of TBS-Tx soluble βCTF (*C*), Aβ40 (*D*) and Aβ42 (*E*) levels by ELISA and MSD multiplex immunoassay in hippocampi from non-injected, controls and AAV-AD rats. A fourth group of AAV-AD rats treated with the Bace1 inhibitor LY2886721 has been also studied. (*F–H*) Comparative analysis of CSF Aβ40 (*F*) and CSF Aβ42 (*G*) levels by MSD multiplex in the same groups previously described. Aβ42 content in hippocampus strongly correlated with CSF Aβ42 (*H*). Bars represent the mean ± SEM. Statistical analyses were performed using 1-way ANOVA followed by Tukey's post hoc test.

dysfunction over time, relative to controls at 3 (n = 20) and 8 months (n = 20) after AD induction. We first analysed anxiety-like emotional behaviour in a new environment using the open-field task, 3 months after AAV-AD induction. The control and AAV-AD rats travelled similar total distances, confirming the absence of motor abnormalities or hyperactivity (Fig. 2*A*). We observed no significant differences in time spent in the centre of the area, despite a downward trend (Control: 3.73 ± 0.93 s; AAV-AD: 1.70 ± 0.62 s; Student's t-test: P = 0.08; Fig. 2*B*). We tested AAV-AD and control rats in the Y-maze and Novel Object Recognition (NOR) tasks to evaluate their working and short-term memories. We observed no differences between the 2 groups (data not shown). Finally, we assessed spatial learning and short and long-term memories using the Morris Water Maze paradigm. There was no difference in the distance travelled to find the hidden platform or the time spent in the target quadrant (data not shown), that contains the platform, during the 5 consecutive training days (Fig. 2*C*). We then performed 3 probe trials to estimate short (4 h after the last trial) and long-term memories (mean of 72 h and 120 h probes; Fig. 2*D*,*E*). We detected no statistical differences between the groups.

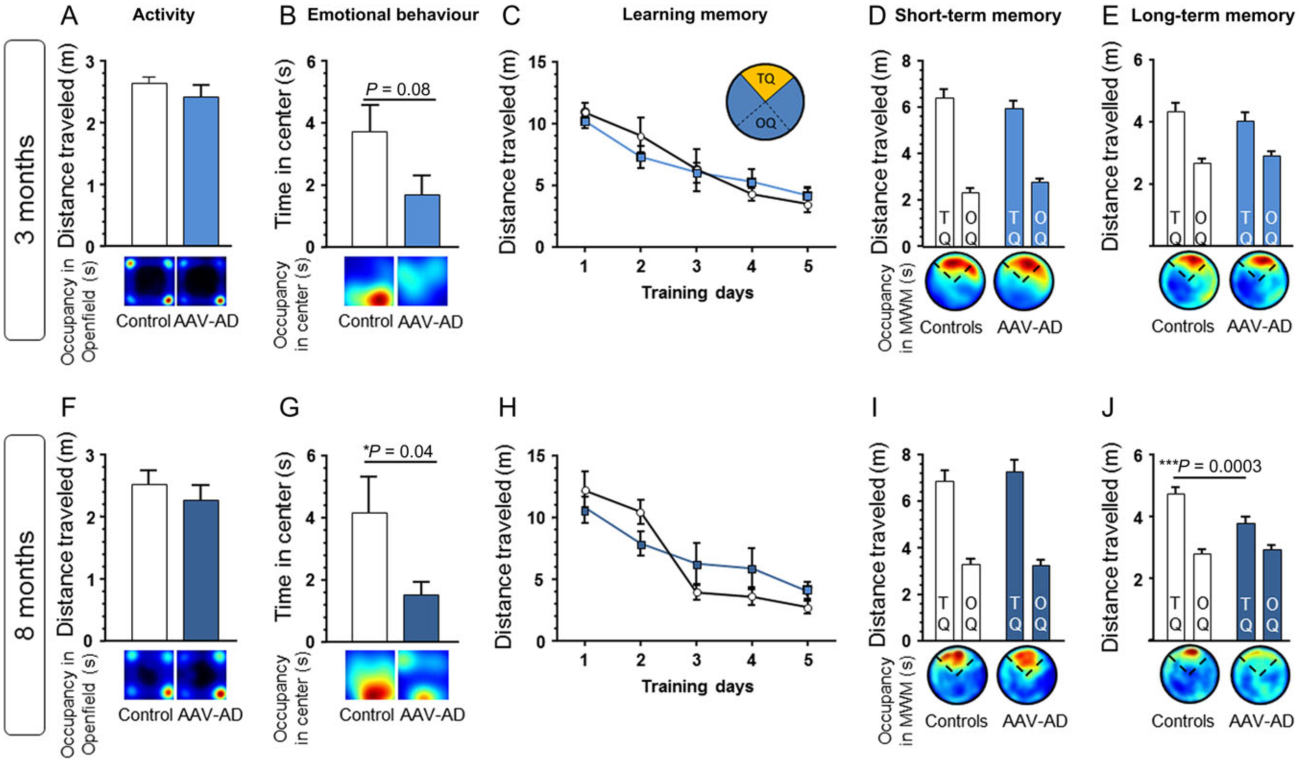

Figure 2. Early emotional disturbances and progressive long-term memory impairment. We evaluated behavioural impairment in AAV-AD rats relative to controls at 3 (*n* = 20) and 8 months (*n* = 20) after AD induction. (*A*, *B*) Open-field assay of 3-months AAV-AD rats. (*A*) Distance travelled during the open-field task. (*B*) Time spent in the centre of the open-field area. (*C–E*) Morris water maze assay of 3-months AAV-AD rats. (*C*) Learning curves representing the travelled distance during the 5 training days in the 4 quadrants (TQ = target quadrant that housed the platform during the training sessions, OQ = mean of other quadrants). (*D*) Probe trial performance at 4 h after the last training session. (*E*) Probe trial performance at 72 h and 120 h after the last training session. (*F–G*) Open-field assay of 8-months AAV-AD rats. (*F*) Distance travelled during the open-field task. (*G*) Time spent in the centre of the open-field area showing a change in emotional behaviour when faced to a new environment in AAV-AD rats. (*H–J*) Morris water maze assay of 8-month AAV-AD rats. (*H*) Travelled distance during the 5 training days in the 4 quadrants. (*I*) Probe trial performance at 4 h after the last training session. (*J*) Probe trial performance at 72 and 120 h after the last training session showing a long-term memory impairment in AAV-AD rats. For each figure, bottom group occupancy plots allow to visualize the areas in which the animals spent the most time during the test. Bars represent the means ± SEM. Statistical analysis were performed using one-way ANOVA followed by Tukey's post hoc test or 2-way ANOVA followed by Sidak's post hoc test depending on the experimental design.

We then tested AAV-AD rats at 8 months after induction using the same approaches. Despite the absence of locomotor hypo-activity (Fig. 2F), AAV-AD rats spent significantly less time in the centre of the open-field apparatus (Control: 4.15 ± 1.17 s; AAV-AD: 1.50 ± 0.43 s; Student's *t*-test: *P* = 0.04; Fig. 2G). We detected no behaviour differences in the Y-Maze or NOR tasks (data not shown). We detected no statistical differences during the learning session and the 4 h probe test (short-term memory; Fig. 2*H*,*I*) of the Morris Water Maze task, but did observe a significant decrease of the mean time spent (long-term memory: Control: 22.40 ± 0.92 s; AAV-AD: 18.54 ± 0.99 s; 2-way ANOVA followed by Sidak's post hoc test: *P* = 0.0064; Supplementary Fig. 1) and mean distance travelled (long-term memory: Control: 4.74 ± 0.22 m; AAV-AD: 3.81 ± 0.18 m; 2-way ANOVA followed by Sidak's post hoc test: *P* = 0.0003; Fig. 2*J*) in the target quadrant during the 72 h/120 h probes. Altogether, AAV-AD rats present emotional and memory impairment between 3 and 8 months postinduction, before both amyloid and phosphorylated Tau aggregations.

Transient Extrasynaptic Deficits Precede LTP Impairment

Here, we evaluated synaptic plasticity and extrasynaptic receptor activation essential for newly formed memories. We first induced LTP at the Schaffer collateral to CA1 pathway by TBS in control (*n* = 13) and AAV-AD (*n* = 16) rats, 3 months after induction (Fig. 3A). We observed no significant difference in LTP between the 2 groups (Student *t*-test: *P* > 0.05), confirmed by the absence of the decrease in Thr 286 phosphorylation of calcium/calmodulin-dependent kinase II (CamkII), implicated in LTP mechanisms (Fukunaga et al. 1995; Lledo et al. 1995) (Fig. 3B). We then performed LTD recordings and again observed no significant differences between the AAV-AD and control groups (Student's *t*-test: *P* > 0.05; Fig. 3C). In parallel, we recorded the tonic current generated in CA1 pyramidal cells by the ambient levels of glutamate acting on extrasynaptic NMDA receptors (NMDAR). The amplitude of the tonic current was significantly greater in the AAV-AD rats than in the control group (Control: 133.8 ± 11.84 pA, *n* = 11; AAV-AD: 213.0 ± 13.60 pA, *n* = 16; Student's *t*-test: *P* = 0.0004; Fig. 3D). We recorded the same parameters in 8-month postinjected rats. AAV-AD rats exhibited significantly lower induction and maintenance of LTPs compared with the control rats (Control: 122.8 ± 3.35%, *n* = 13; AAV-AD: 106.6 ± 4.41%, *n* = 11; Student's *t*-test: *P* = 0.007; Fig. 3E). This LTP impairment was associated with a decrease of CamkII phosphorylation (Control: 1.0 ± 0.02; AAV-AD: 0.72 ± 0.08; Student's *t*-test: *P* = 0.007; Fig. 3F). In contrast, LTD, as the tonic glutamatergic current, was not impaired at this age (Fig. 3*G*,*H*). Altogether, these data suggest that transient extrasynaptic activation occurs before LTP impairment in the early phases.

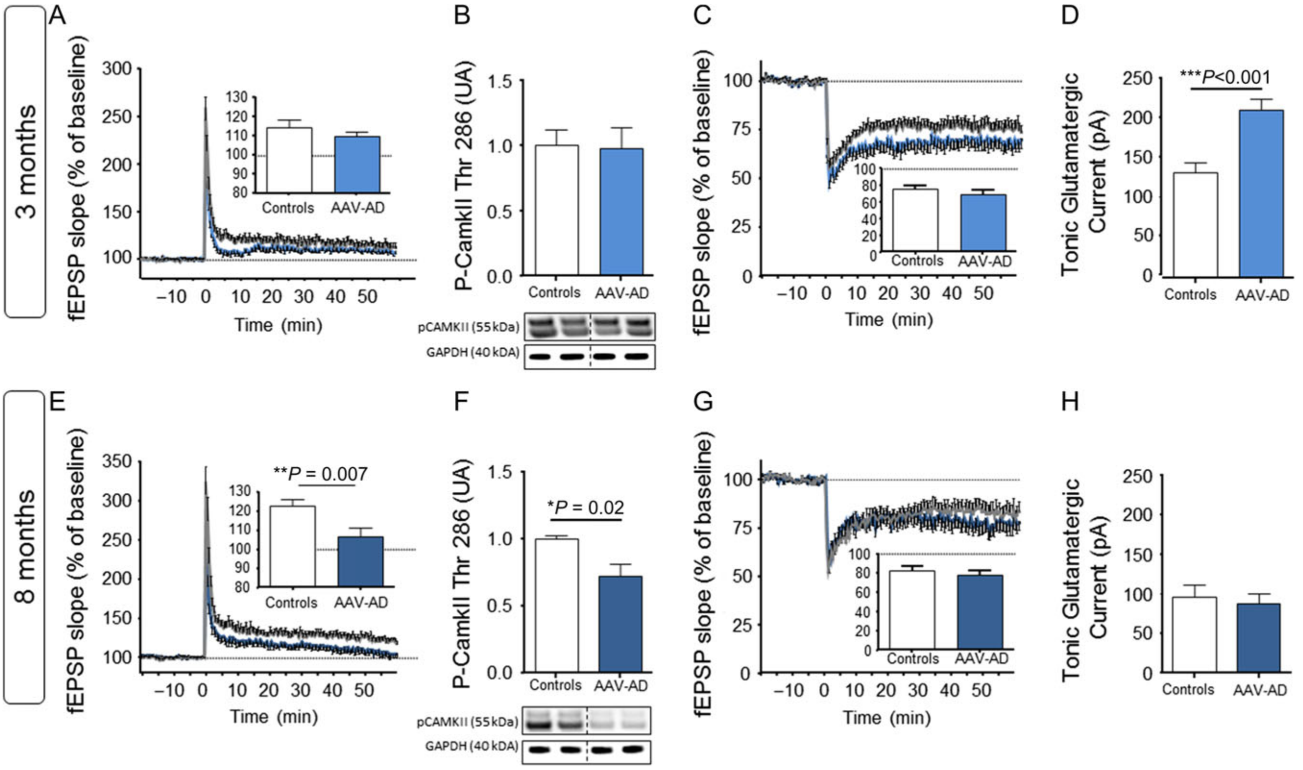

Figure 3. Transient extrasynaptic activation preceded LTP impairment. (*A–D*) Electro-physiological properties of Glutamate receptors, 3 months after AAV-AD induction. The LTP (*A*), the P-CamKII levels (*B*), the long-term depression (LTD, *C*), and the tonic current representing the activation of extrasynaptic NMDA receptors (NMDAR, *D*) were evaluated in 3-month AAV-AD rats (*n* = 10) relative to control rats (*n* = 10). (*E–H*) Electro-physiological properties of Glutamate receptors, 8 months after AAV-AD induction: the LTP (*E*), the P-CamKII levels (*F*), the LTD (*G*), and the activation of extrasynaptic NMDAR (*H*) were quantified in 8-month AAV-AD rats (*n* = 13) compared with control rats (*n* = 13). Bars represent the mean ± SEM. Statistical analyses were performed using the Student's *t*-test.

AAV-AD Rats Develop Progressive AD-Like APP Processing Over Time in the Hippocampus

We established that human APP of AAV-AD rats is processed following the amyloidogenic pathway. We next measured the levels of these metabolites in the hippocampi of AAV-AD rats 1 (*n* = 4), 3 (*n* = 15), 8 (*n* = 15), and 30 months (*n* = 5) after AD induction to evaluate their evolution over time (Fig. 4*A*). These were then compared to those measured in human AD hippocampi (5 age-matched controls + 5 AD Braak 6/Thal 5 patients), which served as a reference. Human APP as total APP levels, did not increase with time in AAV-AD rats (Fig. 4*B*,C). Human APP content was lower in AD cases than in age-matched controls (Student's *t*-test: P = 0.02) and remarkably close to the APP content in the hippocampi of AAV-AD rats (Fig. 4*B*; AAV-AD: 1 month: 1.0 ± 0.28, 3 months: 0.78 ± 0.24, 8 months: 1.13 ± 0.29, 30 months: 0.79 ± 0.18; human controls: 1.77 ± 0.19; AD patients: 1.17 ± 0.10). Similarly, βCTF levels did not increase over time (Fig. 4*D*). We did not observe a significant increase in Aβ40 production, whereas Aβ42 content progressively increased (Fig. 4*E*,*F*; 1 month: 5.93 ± 2.58 pmol/L; 3 months: 11.41 ± 2.75 pmol/L; 8 months: 20.94 ± 4.26 pmol/L; 30 months: 39.26 ± 14.40 pmol/L; 1-way ANOVA: time effect: P = 0.01), leading to a steady increase in the Aβ42/40 ratio in the hippocampi of AAV-AD rats from 1 to 30 months after injection (Fig. 4*G*; 1 month: 0.47 ± 0.02; 3 months: 0.81 ± 0.22; 8 months: 1.45 ± 0.37; 30 months: 3.412 ± 1.41; 1-way ANOVA: time effect: *P* = 0.02). The Aβ40 and Aβ42 content, as well as the Aβ42/40 ratio at 30 months Post-injection were comparable to those observed in the hippocampus of late stage AD patients (Fig. 4*E*,G).

A similar analysis of the CSF confirmed an increase of both human amyloid peptides in AAV-AD rats at 1, 3, and 8 months postinjection (Aβ40:1 month: 2.14 ± 1.02 pg/mL; 3 months: 38.07 ± 4.79 pg/mL; 8 months: 52.23 ± 11.45 pg/mL; Aβ42:1 month: 7.43 ± 3.75 pg/mL; 3 months: 22.44 ± 14.54 pg/mL; 8 months: 46.37 ± 11.54 pg/mL). In contrast, both Aβ40 (37.47 ± 3.65 pg/mL) and Aβ42 (21.89 ± 495 pg/mL) tended to decrease in CSF samples at 30 months postinjection (Fig. 4*H*,*I*). The CSF Aβ42/40 ratio progressed in the opposite direction relative to that of the hippocampus, decreasing over time (Fig. 4*J*; 1 month: 3.40 ± 0.13; 3 months: 1.54 ± 1.32; 8 months: 0.91 ± 0.25; 30 months: 0.60 ± 0.19). In summary, we showed that our model faithfully mimics human amyloid processing (Aβ levels and Aβ42/40 ratio) without APP accumulation in either the hippocampus or CSF.

Human APP Processing Induces a Delayed Metabolism of the Endogenous APP in Rat Hippocampus

We then evaluated the consequences on the endogenous rodent APP processing. Despite absence of differences during the 8 first months, endogenous rat Aβ42 peptides belatedly increased in 30-month-old AAV-AD rat hippocampus relative to age-matched controls (2-way ANOVA followed by Sidak's post hoc test: Interaction effect: P = 0.006; 1 month: ns; 3 months: ns; 8 months: ns; 30 months: P = 0.0005; Supplementary Fig. 2B). By contrast, similar concentrations of rodent Aβ42 peptides was measured in CSF between controls and AAV-AD rats (2-way ANOVA followed by Sidak's post hoc test: Interaction effect: ns; Group effect: ns; Supplementary Fig. 2 C). These results suggest a secondary engagement of the rodent APP

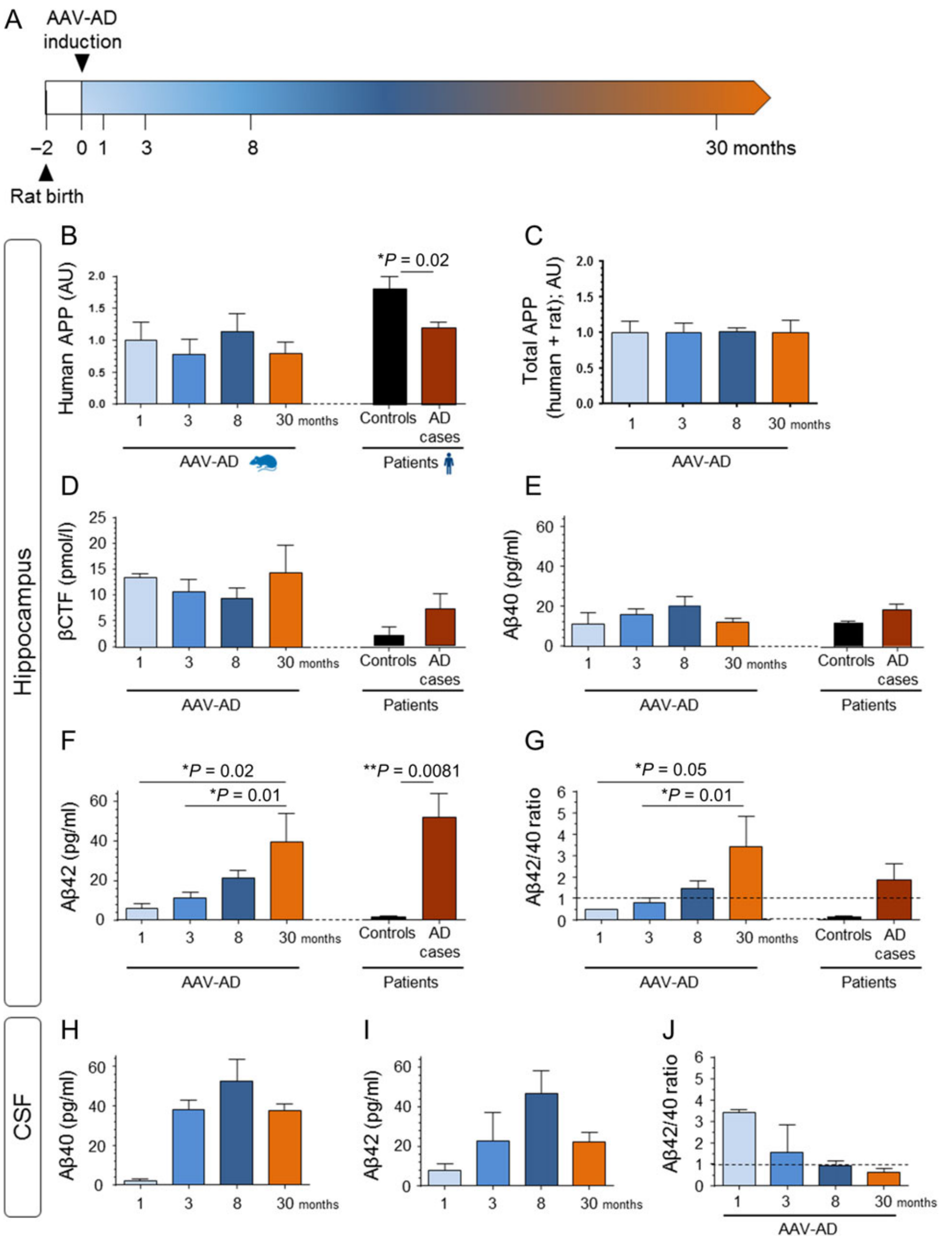

Figure 4. Aβ42/40 ratio increases in hippocampus and decreases in CSF from 1 to 30 months. Metabolites resulting from the amyloidogenic pathway were released into the hippocampus of AAV-AD rats. Rats were killed at 1 (*n* = 4), 3 (*n* = 15), 8 (*n* = 15), and 30 (*n* = 5) months after AAV-AD induction. Human hippocampal samples were obtained from late-onset AD cases (Braak 6, Thal 5, *n* = 5) and age-matched controls (*n* = 5). (*A*) Schematic representation of the experimental design for the progressive AAV-AD rat model. (*B–C*) Densitometric analyses of western blots of human APP (6E10 antibody, *B*) and total APP (rat + human forms; 22C11 antibody, *C*) of the hippocampus of AAV-AD rats for each time-point and for human samples (*n* = 5 per group). (*D–F*) Comparative analysis of TBS-Tx soluble βCTF (*D*), Aβ40 (*E*), and Aβ42 (*F*) levels by Elisa and MSD multiplex respectively. (*G*) Representation of the Aβ42/40 ratio determined by multiplex MSD immunoassay. (*H–I*) Comparative analysis of soluble Aβ40 (*H*) and Aβ42 (*I*) CSF levels by MSD multiplex. (*J*) Representation of the CSF Aβ42/40 ratio over time. Bars represent the means ± SEM. Statistical analyses were performed using 1-way ANOVA followed by Tukey's post hoc test.

processing in the AAV-AD rat hippocampus leaded by the human APP metabolism.

Hippocampal Senile Plaques and CAA Appear at Late Stages in the AAV-AD Rat Model

Most AD animal models develop early amyloid plaques due to massive overexpression of human transgenes, resulting in Aβ accumulation over time that largely exceeds human pathophysiological levels. Here, we evaluated amyloid deposition in AAV-AD rats with several antibodies that detect Aβ. Immunostaining with 4G8, 6E10, and BAM10 antibodies revealed hippocampal amyloid plaques at 30 months postinjection (Fig. 5A). The plaques were mostly located in the subiculum of the hippocampus (Fig. 5B), and were also present at the junction of different tissue layers (Fig. 5C). Nonetheless, we detected plaques at different stages of their formation (Fig. 5D) from diffuse to dense core plaques. Confocal imaging and 3D reconstruction of 4G8 immunostaining lesions confirmed the presence of amyloid lesions in the characteristic form of senile plaques (Fig. 5E). We used 4G8, 6E10, and BAM10

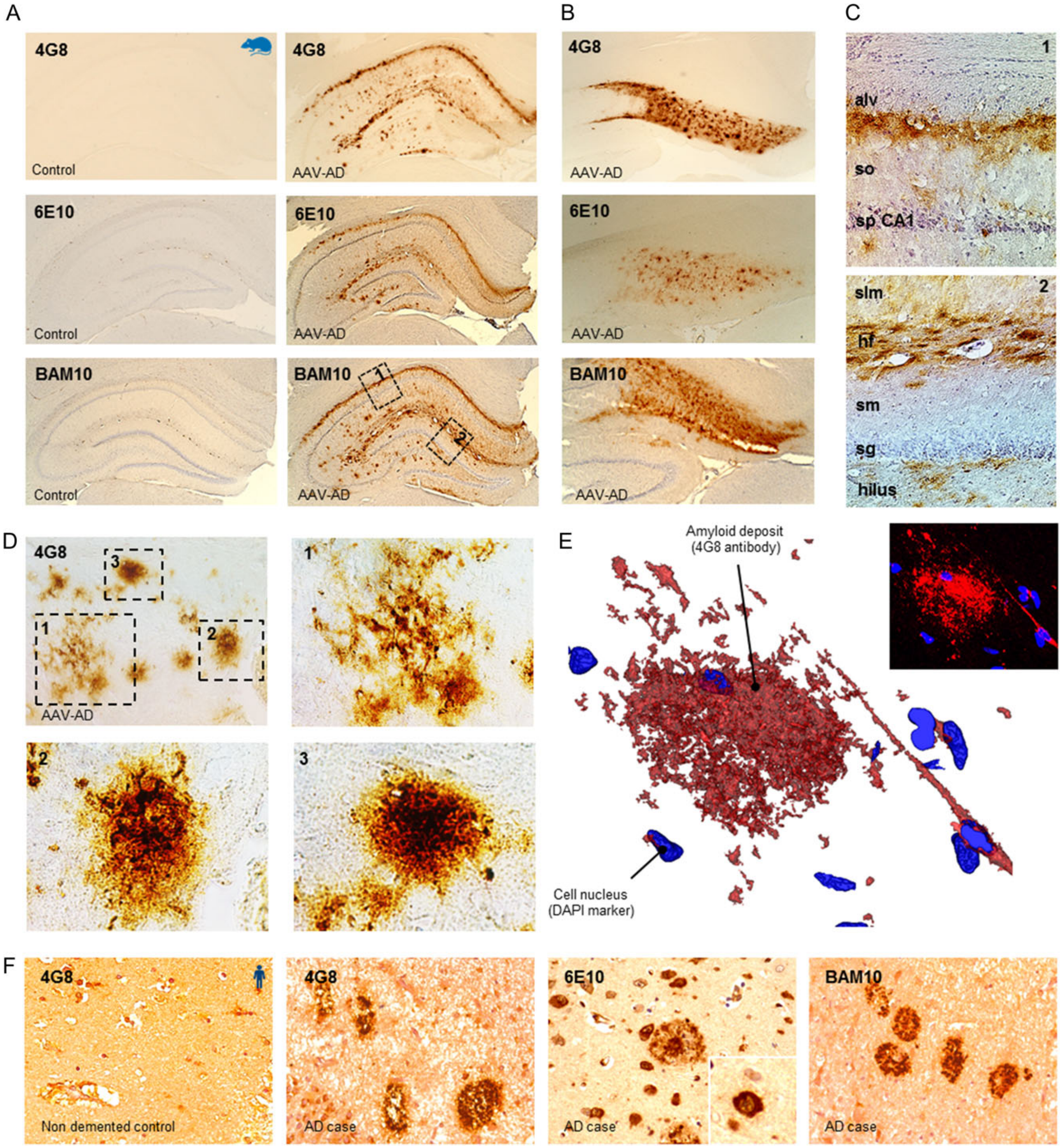

Figure 5. AD-like cerebral amyloid lesions in 30-month-old AAV-AD rats. (*A*) Immunohistochemistry with 4G8, 6E10, and BAM10 antibodies showing amyloid deposition in coronal sections of AAV-AD rat hippocampi. (*B*) Plaque pathology in the subiculum of AAV-AD rats using the antibodies described above. (*C*) Higher magnification of amyloid deposition at the junction of tissue layers. alv, alveus; so, stratum oriens; sp CA1, stratum pyramidale of the CA1 region; slm, stratum lacunosum moleculare; hf, hippocampal fissure; sm, stratum moleculare; sg, stratum granulosum. (*D*) Examples of amyloid plaques at different maturation stages from a diffuse state (box 1) to a dense morphology (box 3). (*E*) 3D reconstruction illustrating the typical form of a 4G8 positive senile plaque in hippocampus of AAV-AD rat. (*F*) Immunohistochemistry with the antibodies described above revealing amyloid plaque lesions in AD patients vs non demented controls.

antibodies to confirm the presence of amyloid deposits in human AD tissue (Fig. 5*F*). We also carried out immunostaining and western blotting for GFAP to analyse potential astrocytic responses induced by amyloid APP processing in the AAV-AD rat model. We did not observe astrogliosis at any time-point after AAV-AD induction (Supplementary Fig. 3).

In order to characterize the cerebral angiopathy in the AAV-AD rat hippocampus, we performed immunostainings with the same previously described antibodies. In 30-month-old AAV-AD rats, we observed characteristic CAA around the blood vessels layers (Fig. 6*A*). In order to better characterize the vessel-surrounding aggregation, we proceed to a double

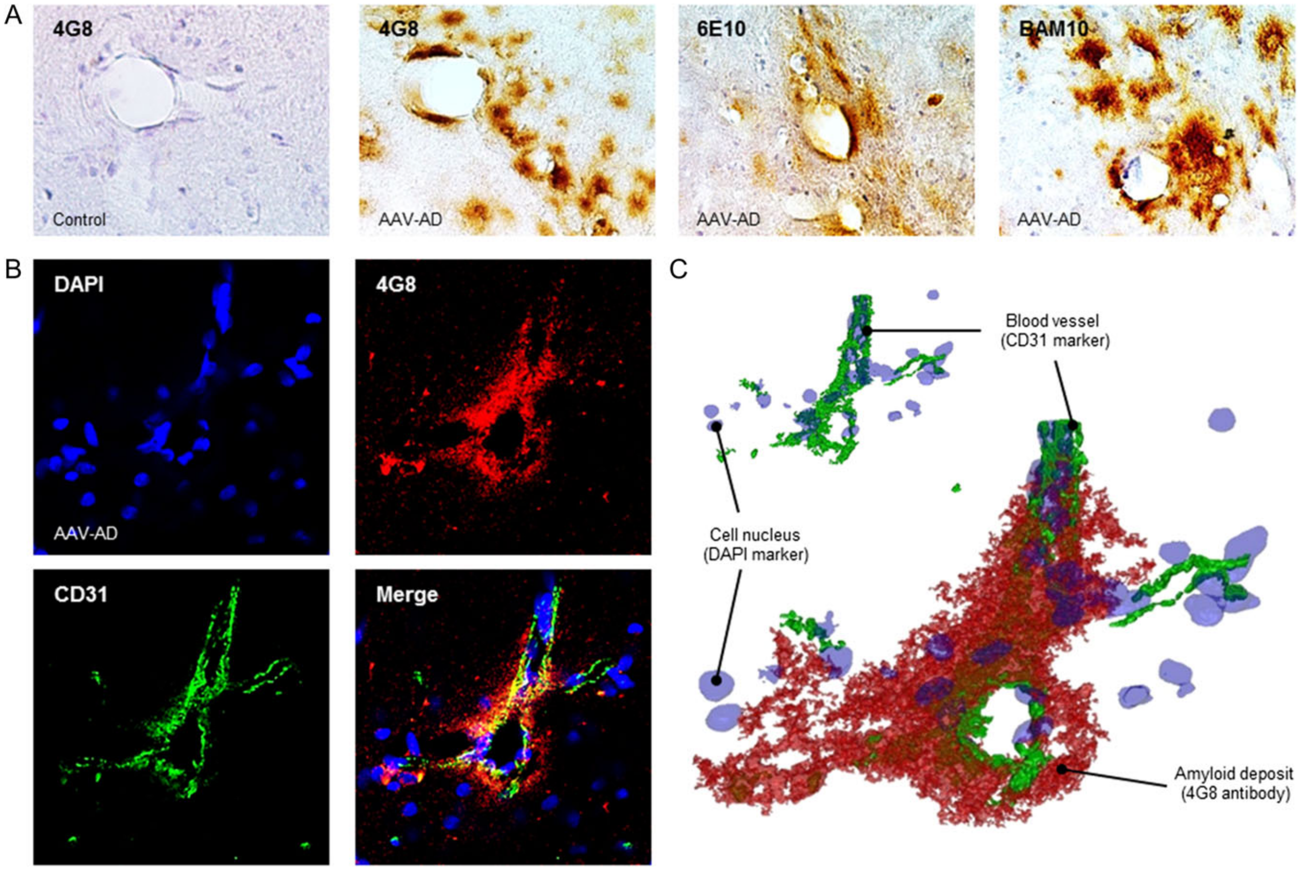

Figure 6. APP processing triggers CAA in 30-month-old AAV-AD rats. (*A*) Immunohistochemistry with 4G8, 6E10, and BAM10 antibodies showing respectively endogenous and exogenous CAA in coronal sections of AAV-AD rat hippocampi. (*B*) Laser confocal microscopy showing aggregation of endogenous amyloid (4G8) surrounding cerebral vessel identified with endothelial cells marker (CD31) in coronal sections of AAV-AD rat. (*C*) 3D reconstruction illustrating the CAA in sections of AAV-AD rat.

staining with both 4G8 and CD31 (a vessel marker) antibodies (Fig. 6*B*). Thus, we observed a blood vessel-surrounding amyloid sheath, observation confirmed by the 3D reconstruction (Fig. 6*C*). Altogether, these data indicate that a model exhibiting a slow progression to the AD phenotype can provide information about the initiation of amyloid deposition in the brain parenchyme as plaques and around vessels as CAA.

Progressive Hyper- and Abnormal Phosphorylations of the Endogenous Tau Protein

We analysed the consequences of the amyloidogenic pathway on the phosphorylation of Tau. We used 4 different approaches (ELISA, western blot, HPLC and MSD multiplex immunoassay) to evaluate the phosphorylation of the endogenous Tau protein (P-Tau) on both hyperphosphorylated (thr181, thr212, thr217, thr202, thr231/235, and thr231) or abnormally phosphorylated sites (ser 422) (Augustinack et al. 2002) at 1 ($n = 5$), 3 ($n = 5$), 8 ($n = 5$), and 30 months ($n = 5$) postinduction. The global trend of Tau phosphorylation was equivalent for each studied phosphorylated site, and gradually increased over time relative to age-matched controls (Fig. 7*A*) (Time effect: thr181: $P < 0.001$, thr212: $P < 0.002$, thr217: $P = 0.07$, thr202: $P < 0.04$, thr231/235: $P = 0.\ 21$, ser 422: $P < 0.0001$ and thr231: $P < 0.001$; Group effect: thr181: $P < 0.05$, thr212: $P < 0.001$, thr217: $P = 0.04$, thr202: $P < 0.03$, thr231/235: $P = 0.\ 08$, ser 422: $P < 0.0001$ and thr231: ns; Interaction effect: thr181: $P = 0.05$, thr212: $P < 0.001$, thr217: $P = 0.05$, thr202: $P < 0.04$, thr231/235: $P = 0.\ 08$, ser 422: $P < 0.0001$, and thr231: $P < 0.001$). The thr181 and ser422 epitopes early appeared to be phosphorylated by 8 months (thr181: Control: 69.8 ± 7.48 pg/mL; AAV-AD: 124.30 ± 12.01 pg/mL; 2-way ANOVA followed by Sidak's post hoc test $P < 0.001$; ser422: Control: 1.00 ± 0.28; AAV-AD: 1.96 ± 0.14; 2-way ANOVA followed by Sidak's post hoc test $P = 0.017$). Moreover, the phosphorylation of all studied epitopes was higher than in age-matched controls by 30 months after AAV-AD induction (2-way ANOVA followed by Sidak's post hoc test: thr181: $P = 0.06$, thr217: $P = 0.005$, thr202: $P = 0.002$, thr231/235: $P = 0.\ 04$, ser422: $P < 0.0001$, thr212: $P < 0.001$, and thr231: $P < 0.001$) (Fig. 7*B*,*C*).

Biochemical assessment of hippocampus samples using AT8 and AT100 antibodies confirmed the hyper- and abnormal phosphorylation of the endogenous Tau protein but only in half of 30-month-old AAV-AD rats (Fig. 7*D*). Thus, western blotting revealed characteristic bands close to 80 kDa using both antibodies in these animals. Interestingly these antibodies are currently used in clinics to deliver a definitive diagnosis in postmortem brain samples because of their capacity to mark tangles structures. Finally, we evaluated 3 kinases involved in the AD phosphorylation of Tau by western blotting: cyclin-dependent kinase 5 (CDK5), glycogen synthase kinase 3β (GSK3β), and Dual specificity tyrosine-phosphorylation-regulated kinase 1A (DYRK1A). We observed a continuous increase of GSK3β and DYRK1A levels from 1 to 30 months postinduction (2-way ANOVA: Time effect: GSK3β: $P < 0.0036$ and DYRK1A: $P < 0.001$), whereas CDK5 levels remained stable (2-way ANOVA: Time effect: $P = 0.14$) (Fig. 7*E*,*F*; Supplementary Fig. 4).

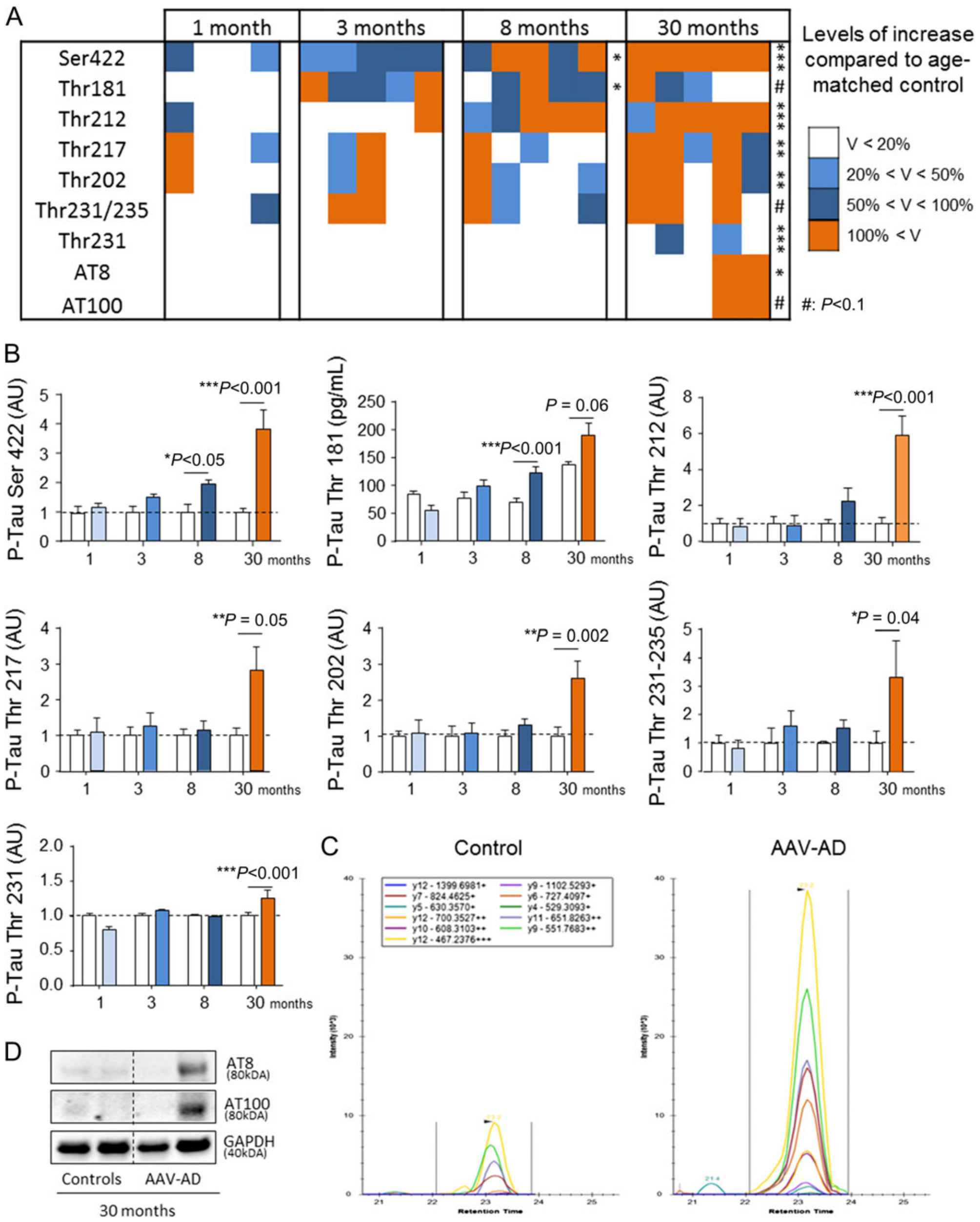

Figure 7. APP processing triggers sequential endogenous hyper- and abnormal Tau phosphorylation from 8 months postinjection. (*A* and *B*) Comparative analysis of TBS-Tx soluble rat phosphorylated Tau protein at residue Ser422, Thr212 (by western blot), Thr181 (by ELISA), Thr217, Thr, 202, 231-235 (by HPLC), and Thr231 (by MSD immunoassay). (*C*) LC-MS/MS signal of phosphorylated Thr 217 peptide ion fragments used for quantification in hippocampal samples from 30-month-old AAV-AD rat and age-matched control. (*D*) Representative western blot showing both AT8 and AT100 bands in AAV-AD rats hippocampi. (*E*, *F*) Densitometric analyses of western blots showing the expression of CDK5, GSK3β, and DYRK1A in each group and at different time points (*n* = 5 rats per group). Bars represent the means ± SEM. Statistical analyses were performed using 2-way ANOVA followed by Sidak's post hoc test.

Hippocampal Tangle-Like Aggregates Appeared at Late Stages in the AAV-AD Rat Model

We performed immunohistochemistry with the AT8 (hyperphosphorylated epitopes: ser202/thr205) and AT100 (abnormal epitopes: thr212/ser214) antibodies to assess the potential aggregation of phosphorylated Tau measured in 30 months AAV-AD rats. We observed AT8 and AT100 positive cells in the *hilus* and *subiculum* (Fig. 8*A*). Strikingly, we observed a very similar pattern in hippocampal slices of AD patients, displaying AT8 and AT100 positive core dense cells (Fig. 8*B*). Confocal imaging and 3D reconstruction of AT8 immunostaining confirmed the presence of hyperphosphorylated endogenous Tau surrounding nucleus in the characteristic form of misfolded protein aggregates (Fig. 8*C*,*D*). All these compelling data demonstrate that continuous human-like βAPP processing during years induces accretion of phosphorylated Tau protein into tangle-like aggregates.

Discussion

Understanding the infra-clinical phases and finding new early biomarkers will be decisive in the development of effective

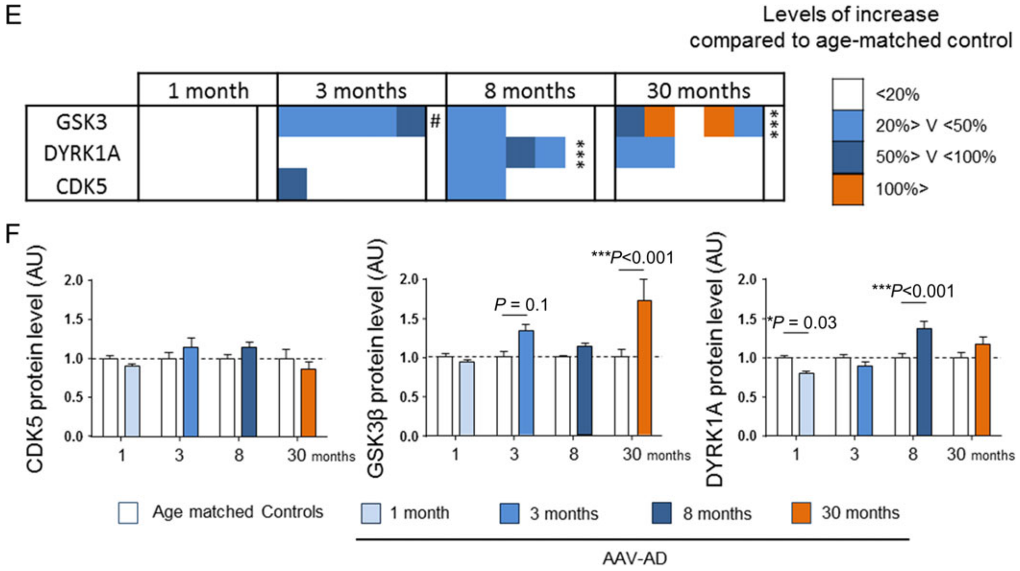

Figure 7. *Continued.*

preventive or therapeutic molecules to counteract AD (Langbaum et al. 2013). It is thus essential to dispose models that closely mimic human AD whether on the evolution over time or on the amyloid peptides levels produced (Sala Frigerio and De Strooper 2016). To address this challenge, we developed an original AD rat model by co-transfer of the APP_{SL} and $PS1_{M146L}$ genes using hippocampal AAV vector delivery. This model shows a specific age-dependent progression pattern. Longitudinal analysis of this model has allowed us to experimentally confirm the causal relationship between human-like βAPP processing and Tau pathology including Tau tangle-like aggregation in order to propose a 4-step hypothesis of prodromal AD progression (Fig. 9).

We generated AAV vectors encoding mutated human $PS1_{M146L}$ or APP_{SL}, which were bilaterally injected into young adult rat hippocampus to generate the AAV-AD rat model. AAV-$PS1_{M146L}$ injected rats were used as controls. AAV-AD rats produced APP from 1-month after vector injection. Human APP immunoreactivity was found in sparse neurons of the CA2/CA3 layers, subiculum, and dentate gyrus. This pattern of expression may mimic the genomic mosaicism recently described in sporadic forms of human AD, in which an increase in copy number was observed for the APP gene in a limited subset of neurons (Bushman et al. 2015). The absence of APP accumulation in the hippocampus of AAV-AD rats, which was at levels similar to those in both control rats and AD patients, suggests that human APP was quickly catabolized by the β-secretase complex. This was corroborated by the rapid effect of the BACE inhibitor observed in less than 4 h. Moreover, βCTF, Aβ40, and Aβ42 peptides were produced in the hippocampus from 1-month after AAV-AD induction, whereas the levels of APP remained unchanged (Fig. 9, Step 1). Reducing Aβ42 peptides levels or normalizing the Aβ42/40 ratio by inhibiting amyloid APP processing appears to be the best therapeutic strategy at this first step of disease progression.

The concentration of soluble Aβ42 and the Aβ42/40 ratio gradually increased over time, whereas βCTF and Aβ40 levels remained stable. By 30 months after induction, the relative amount of Aβ in the brains of the rats was similar to that found in AD patients. Analysis of the CSF revealed Aβ diffusion from the hippocampus to the CSF. In contrast to the increased hippocampal Aβ42/40 ratio, the CSF Aβ42/40 ratio progressively decreased over time (Fig. 9, Step 1). These data suggest that the ability of soluble Aβ42 to spread from the hippocampus to the CSF decreased over time, leading to an increase in Aβ42 levels in the hippocampus and a reduction in the CSF. This may be due to progressive CAA leading to endothelial membrane modifications as we observed in 30-month AAV-AD rats: as the level of vascular angiopathy increases, so does the level of Aβ42 in the hippocampus, whereas it decreases in the CSF (Ikeda et al. 2012). However, some therapeutic strategies (i.e., Aβ immunotherapy) developed to remove cerebral Aβ42 aggregates also increase the severity of CAA (Patton et al. 2006; Weller et al. 2009). Strategies that prevent vascular amyloidosis and rebalance hippocampal and CSF Aβ ratios may be beneficial (Agyare et al. 2014).

Emotional behaviour was altered without memory defects within 3 months after induction (Fig. 9, step 2). This observation suggests that there may be specific emotional neuropsychological disturbances that could be used as a potential readout in clinic practice as a very early cognitive symptom in AD patients (McCade et al. 2011).

The amplitude of the tonic current was greater in AAV-AD rats 3 months after induction as a direct consequence of AAV-AD induction. Progression of the disease resulted in secondary normalization of extrasynaptic NMDA receptor (eNMDAR) activation. Accordingly, transient extrasynaptic alterations appeared shortly after the Aβ42-induced neuronal stress. Such observations have already been described after the application of Aβ42 to mixed neuronal/glial rat cerebrocortical cultures (Talantova et al. 2013). Several events, such as a decrease of scaffolding proteins, a reduction of the glutamate transporter GLT-1, or an increase in glutamate liberation by astrocytes can lead to increased stimulation of the eNMDARs (Masliah et al. 1996; Li et al. 2011). Extrasynaptic NMDA receptor activation is implicated in the pathogenesis of several CNS disorders and Aβ disturbs the balance between synaptic and eNMDAR activation (Wang et al. 2013). We show here, for the first time in vivo in our knowledge, that these transient events appear at the earliest stages of the disease course, before the onset of classical hallmarks such as amyloid plaques, neurofibrillary tangles or memory and LTP impairment (Fig. 9, step 2).

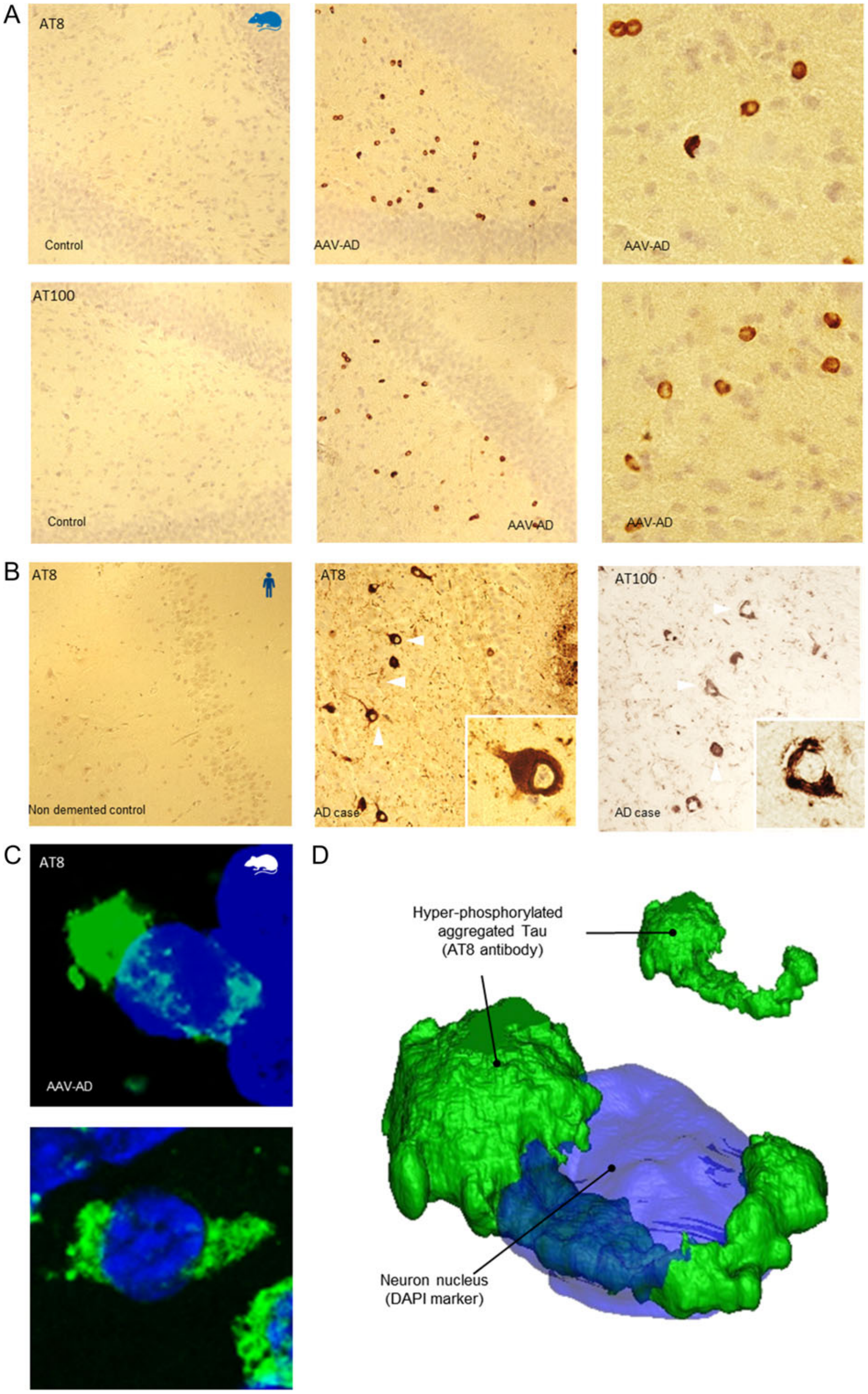

Figure 8. APP processing triggers terminal endogenous phosphorylated Tau aggregation in 30-month-old AAV-AD rats. (*A*) Immunohistochemistry with AT8 and AT100 antibodies showing respectively pretangle and tangle neurons located in the hilus of the DG in AAV-AD rat coronal sections. (*B*) Immunohistochemistry with AT8 and AT100 antibodies showing respectively pretangle and tangle lesions in AD patients. (*C*) Laser confocal microscopy showing AT8 positive cells in coronal sections of AAV-AD rat. (*D*) 3D reconstruction illustrating the typical helicoidal form of an AT8 positive pretangle neuron in hippocampus of AAV-AD rat.

The third step of AD progression may be related to the first memory problems in patients before clinical diagnosis (Rajan et al. 2015). We evaluated the LTP of glutamate synaptic transmission in AAV-AD rats at 3 and 8 months postinduction. We observed no defects in LTP in 3-month AAV-AD rats. In contrast, a large decrease in LTP may be attributable to AD progression in 8-month AAV-AD rats (Fig. 9, step 3). Long-term memory was intact 3 months after induction, as opposed to after 8 months, in which the AAV-AD rats displayed memory impairment (Fig. 9, step 3). Indeed, we observed long-term memory impairment in association with LTP defects from 8 months postinduction and later, suggesting progressive memory disturbances.

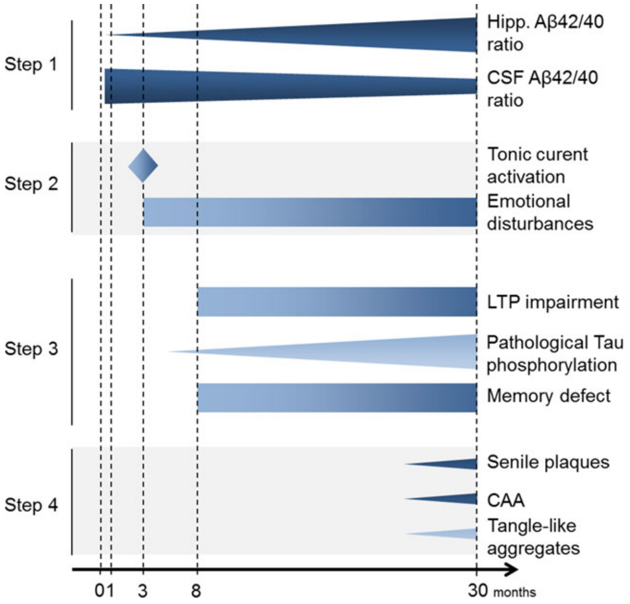

Figure 9. Age-dependent progression of pre-clinical AD stages: the 4-steps hypothesis.

We then investigated the potential impact of the amyloidogenic pathway on endogenous Tau phosphorylation. ELISA analysis demonstrated higher levels of Tau protein phosphorylation on residues thr181 and ser422 in the AAV-AD rat hippocampus than in control rats, from 8 months postinduction. These results confirm that the continuous increase of Aβ levels, resulting from APP processing, was sufficient to trigger Tau pathway engagement as observed in AD patients (Fig. 9, step 3) (Selkoe and Hardy 2016). In addition, this engagement of the Tau pathway was associated with an increased level of specific kinases, such as GSK3β and DYRK1A. Strikingly, almost all amyloid transgenic mice do not develop progressive tau pathology in the brain (Kitazawa et al. 2012). Based on these experimental results, rejection of the amyloid cascade hypothesis was suggested arguing that pathological APP processing is not sufficient to drive tau pathology in rodent brain. However, our results clearly link APP and Tau pathologies and strengthens the amyloidogenic cascade hypothesis.

The next phase of AD disease progression consists of the appearance of AD-related cerebral lesions. Senile plaques and tangle-like aggregates appeared in AAV-AD hippocampus at least 30 months after AAV-AD induction (Fig. 9, step 4). These findings confirm the role of gradually increasing levels of the soluble forms of Aβ, and potentially the Aβ42/40 ratio, starting from adulthood in both senile plaque and tangle formation, several years after induction. This may explain, in part, why subtle cognition/biological defects are present at least 18 years before clinical diagnosis (Rajan et al. 2015). Our results are once again in agreement with the evolution of the disease in humans. Thus, in experimental models with APP pathology close to AD patient, senile plaque were associated with Tau aggregation process as observed in AD brains. Unfortunately, it was not possible to observe the following steps of AD progression using AAV-AD rats because of their limited lifespan. It is possible that step 4 correspond to the time of AD diagnosis in patients.

How to explain that AAV-AD rats develop both APP and Tau pathologies while usual amyloid models failed? This main difference compared to classic AD models could be explained by the technology used. Because induction is realized on adult animals, AAV-AD rats do not suffer from developmental compensation that could result in neuroprotection mechanisms breaking down Tau pathology. Another argument could be that induced APP pathology appear similar to human in terms of amyloid peptides amounts and Aβ42/40 ratio resulting in pathophysiology mechanisms including Tau pathology. The last difference lies in slow progression in setting the APP pathology, allowing time for Tau pathology development without early inflammation and plaque formation interfering.

In summary, this study reports the first experimental demonstration of amyloid cascade in rodents thanks to an inducible progressive AD rat model named AAV-AD rat. We propose a 4-step hypothesis for infra-clinical AD progression based on the study of the AAV-AD model over time. Step 1 consists of the enhancement of APP processing resulting in a steady increase of Aβ42 levels and the Aβ42/40 ratio in the hippocampus starting from adulthood. Step 2 is characterized by the transient activation of extrasynaptic glutamate receptors and the onset of altered emotional behaviour. During Step 3, classical biological alterations gradually appear such as a defect in LTP, hyperphosphorylation of endogenous Tau, and long-term memory deficits. Finally, old AAV-AD rats develop specific histological lesions consisting of amyloid plaques and tangle-like aggregates (Fig. 9, step 4). This 4-step hypothesis highlights the need for pleiotropic therapies acting at least on both amyloid and Tau pathologies. Our AAV-AD rat model may be a flexible in vivo experimental setting to increase the understanding of AD onset, identify early AD biomarkers, while evaluating the efficacy of therapeutic strategies to counteract AD progression.

Authors' Contributions

M.A., B.S., and J.B. carried out the design of the study and wrote the manuscript. M.A., B.S., and J.B. performed the biochemical, behavioural, histological, and statistical analyses. R.F., S.A., N.S.O., S.T. participated in the biochemical analyses and helped to draft the manuscript. Y.A. helped for the Bace1 inhibitor experiment as well as the behavior. S.A. performed the immunostaining on human slices. P.D., B.P., J.-M.B. and A.H. performed the electro-physiological recordings and helped to design the study and draft the manuscript. A.V. and F.B. realized the HPLC experiments. T.D. performed the 3D reconstruction. A.-P.B. and C.J. helped with the viral production. N.C., P.H. and N.D. read the manuscript. All authors read and approved the final manuscript.

Supplementary Material

Supplementary data are available at *Cerebral Cortex* online.

Funding

This work was supported by DIM Biotherapies, the Région Ile-de-France, IDEX Paris Saclay, INSERM Transfert, CEA "Technologie Pour la Santé" and by a grant from "Investissement d'Avenir—ANR-11-INBS-0011"—NeurATRIS: A Translational Research Infrastructure for Biotherapies in Neurosciences. Human postmortem samples were obtained from the GIE-Neuro-CEB brain bank, which is run by a consortium of patient associations.

Notes

We thank Noëlle Dufour, and Gwenaëlle Auregan for their help in producing the viral vectors, Gaëlle Dufayet-Chaffaud for her help in the biochemical analyses, and Karine Cambon for advice on animal behaviour. *Conflict of interest*: The authors have no competing financial interests to declare.

References

Abbott A. 2004. Laboratory animals: the Renaissance rat. Nature. 428:464–466.

Agyare EK, Jaruszewski KM, Curran GL, Rosenberg JT, Grant SC, Lowe VJ, Ramakrishnan S, Paravastu AK, Poduslo JF, Kandimalla KK. 2014. Engineering theranostic nanovehicles capable of targeting cerebrovascular amyloid deposits. J Control Release. 185:121–129.

Alves S, Bode J, Bemelmans A-P, Kalle Von C, Cartier N, Tews B. 2016. Ultramicroscopy as a novel tool to unravel the tropism of AAV gene therapy vectors in the brain. Sci Rep. 6:28272.

Audrain M, Fol R, Dutar P, Potier B, Billard J-M, Flament J, Alves S, Burlot M-A, Dufayet-Chaffaud G, Bemelmans A-P, et al. 2016. Alzheimer's disease-like APP processing in wild-type mice identifies synaptic defects as initial steps of disease progression. Mol Neurodegener. 11:5.

Augustinack JC, Schneider A, Mandelkow E-M, Hyman BT. 2002. Specific tau phosphorylation sites correlate with severity of neuronal cytopathology in Alzheimer's disease. Acta Neuropathol. 103:26–35.

Barthélemy NR, Fenaille F, Hirtz C, Sergeant N, Schraen-Maschke S, Vialaret J, Buée L, Gabelle A, Junot C, Lehmann S et al. 2016. Tau Protein Quantification in Human Cerebrospinal Fluid by Targeted Mass Spectrometry at High Sequence Coverage Provides Insights into Its Primary Structure Heterogeneity. J Proteome Res. 15(2):667–676.

Berger A, Lorain S, Josephine C, Desrosiers M, Peccate C, Voit T, Garcia L, Sahel JA, Bemelmans AP. 2015. Repair of Rhodopsin mRNA by Spliceosome-Mediated RNA Trans-Splicing: A New Approach for Autosomal Dominant Retinitis Pigmentosa. Mol Ther. 23:918–30.

Bushman DM, Kaeser GE, Siddoway B, Westra JW, Rivera RR, Rehen SK, Yung YC, Chun J. 2015. Genomic mosaicism with increased amyloid precursor protein (APP) gene copy number in single neurons from sporadic Alzheimer's disease brains. eLife. 4:e05116.

Do Carmo S, Cuello AC. 2013. Modeling Alzheimer's disease in transgenic rats. Mol Neurodegener. 8:37.

Dubois B, Feldman HH, Jacova C, Hampel H, Molinuevo JL, Blennow K, DeKosky ST, Gauthier S, Selkoe D, Bateman R, et al. 2014. Advancing research diagnostic criteria for Alzheimer's disease: the IWG-2 criteria. Lancet Neurol. 13:614–629.

Echeverria V, Ducatenzeiler A, Alhonen L, Janne J, Grant SM, Wandosell F, Muro A, Baralle F, Li H, Duff K, et al. 2004. Rat transgenic models with a phenotype of intracellular Abeta accumulation in hippocampus and cortex. J Alzheimers Dis. 6:209–219.

Ferreira ST, Lourenco MV, Oliveira MM, De Felice FG. 2015. Soluble amyloid-β oligomers as synaptotoxins leading to cognitive impairment in Alzheimer's disease. Front Cell Neurosci. 9:191.

Flood DG, Lin Y-G, Lang DM, Trusko SP, Hirsch JD, Savage MJ, Scott RW, Howland DS. 2009. A transgenic rat model of Alzheimer's disease with extracellular Abeta deposition. Neurobiol Aging. 30:1078–1090.

Fol R, Braudeau J, Ludewig S, Abel T, Weyer SW, Roederer J-P, Brod F, Audrain M, Bemelmans A-P, Buchholz CJ, et al. 2015. Viral gene transfer of APPsα rescues synaptic failure in an Alzheimer's disease mouse model. Acta Neuropathol. 131: 247–266.

Folkesson R, Malkiewicz K, Kloskowska E, Nilsson T, Popova E, Bogdanovic N, Ganten U, Ganten D, Bader M, Winblad B, et al. 2007. A transgenic rat expressing human APP with the Swedish Alzheimer's disease mutation. Biochem Biophys Res Commun. 358:777–782.

Fukunaga K, Muller D, Miyamoto E. 1995. Increased phosphorylation of Ca2+/calmodulin-dependent protein kinase II and its endogenous substrates in the induction of long-term potentiation. J Biol Chem. 270:6119–6124.

Hardy JA, Higgins GA. 1992. Alzheimer's disease: the amyloid cascade hypothesis. Science. 256:184–185.

Ikeda M, Hirayanagi K, Arai M, Kakuda S, Makioka K, Furuta N, Takai E, Kasahara H, Tsukagoshi S, Fujita Y, et al. 2012. Encephalopathy with amyloid angiopathy and numerous amyloid plaques with low levels of CSF Aβ1-40/Aβ1-42. Amyloid. 19:186–190.

Kitazawa M, Medeiros R, LaFerla FM. 2012. Transgenic mouse models of Alzheimer disease: developing a better model as a tool for therapeutic interventions. Curr Pharm Des. 18: 1131–1147.

Langbaum JB, Fleisher AS, Chen K, Ayutyanont N, Lopera F, Quiroz YT, Caselli RJ, Tariot PN, Reiman EM. 2013. Ushering in the study and treatment of preclinical Alzheimer disease. Nat Rev Neurol. 9:371–381.

Lee J-E, Han P-L. 2013. An update of animal models of Alzheimer disease with a reevaluation of plaque depositions. Exp Neurobiol. 22:84–95.

Leon WC, Canneva F, Partridge V, Allard S, Ferretti MT, DeWilde A, Vercauteren F, Atifeh R, Ducatenzeiler A, Klein W, et al. 2010. A novel transgenic rat model with a full Alzheimer's-like amyloid pathology displays pre-plaque intracellular amyloid-beta-associated cognitive impairment. J Alzheimers Dis. 20:113–126.

Li S, Jin M, Koeglsperger T, Shepardson NE, Shankar GM, Selkoe DJ. 2011. Soluble Aβ oligomers inhibit long-term potentiation through a mechanism involving excessive activation of extrasynaptic NR2B-containing NMDA receptors. J Neurosci. 31:6627–6638.

Lledo PM, Hjelmstad GO, Mukherji S, Soderling TR, Malenka RC, Nicoll RA. 1995. Calcium/calmodulin-dependent kinase II and long-term potentiation enhance synaptic transmission by the same mechanism. Proc Natl Acad Sci USA. 92: 11175–11179.

Masliah E, Alford M, DeTeresa R, Mallory M, Hansen L. 1996. Deficient glutamate transport is associated with neurodegeneration in Alzheimer's disease. Ann Neurol. 40: 759–766.

McCade D, Savage G, Naismith SL. 2011. Review of emotion recognition in mild cognitive impairment. Dement Geriatr Cogn Disord. 32:257–266.

Patton RL, Kalback WM, Esh CL, Kokjohn TA, Van Vickle GD, Luehrs DC, Kuo Y-M, Lopez J, Brune D, Ferrer I, et al. 2006. Amyloid-beta peptide remnants in AN-1792-immunized Alzheimer's disease patients: a biochemical analysis. Am J Pathol. 169:1048–1063.

Rajan KB, Wilson RS, Weuve J, Barnes LL, Evans DA. 2015. Cognitive impairment 18 years before clinical diagnosis of Alzheimer disease dementia. Neurology. 85:898–904.

Ruiz-Opazo N, Kosik KS, Lopez LV, Bagamasbad P, Ponce LR, Herrera VL. 2004. Attenuated hippocampus-dependent learning and memory decline in transgenic TgAPPswe Fischer-344 rats. Mol Med. 10:36–44.

Sala Frigerio C, De Strooper B. 2016. Alzheimer's Disease Mechanisms and Emerging Roads to Novel Therapeutics. Annu Rev Neurosci. 39:57–79.

Selkoe DJ. 2002. Alzheimer's disease is a synaptic failure. Science. 298:789–791.

Selkoe DJ, Hardy J. 2016. The amyloid hypothesis of Alzheimer's disease at 25 years. EMBO Mol Med. 8:595–608.

Talantova M, Sanz-Blasco S, Zhang X, Xia P, Akhtar MW, Okamoto S-I, Dziewczapolski G, Nakamura T, Cao G, Pratt AE, et al. 2013. Aβ induces astrocytic glutamate release, extrasynaptic NMDA receptor activation, and synaptic loss. Proc Natl Acad Sci USA. 110:E2518–E2527.

Wang ZC, Zhao J, Li S. 2013. Dysregulation of synaptic and extrasynaptic N-methyl-D-aspartate receptors induced by amyloid-beta. Neurosci Bull. 29:752–760.

Weller RO, Boche D, Nicoll JAR. 2009. Microvasculature changes and cerebral amyloid angiopathy in Alzheimer's disease and their potential impact on therapy. Acta Neuropathol. 118:87–102.